



Research Paper

3D human stem-cell-derived neuronal spheroids for *in vitro* neurotoxicity testing of methylglyoxal, highly reactive glycolysis byproduct and potent glycating agent

Teresa Coccini^{a,*}, Francesca Caloni^b, Luciana Alessandra Russo^c, Laura Villani^c, Davide Lonati^a, Uliana De Simone^a

^a Istituti Clinici Scientifici Maugeri IRCCS, Laboratory of Clinical and Experimental Toxicology, and Pavia Poison Centre-National Toxicology Information Centre, Toxicology Unit, Pavia, Italy

^b Dipartimento di Scienze e Politiche Ambientali (ESP), Università degli Studi di Milano, Milan, Italy

^c Istituti Clinici Scientifici Maugeri IRCCS, Pathology Unit, Pavia, Italy

ARTICLE INFO

Keywords:

Human stem-cell-derived neurons
Umbilical cord
In vitro three-dimensional cell-based model
Glycotoxins
Neurodegeneration
Aging
Dicarbonyl stress
Advanced glycation end-products (AGEs)

ABSTRACT

Human-derived three-dimensional (3D) *in vitro* models are advanced *human cell-based* model for their complexity, relevance and application in toxicity testing. Intracellular accumulation of methylglyoxal (MGO), the most potent glycating agent in humans, mainly generated as a by-product of glycolysis, is associated with age-related diseases including neurodegenerative disorders.

In our study, 3D human stem-cell-derived neuronal spheroids were set up and applied to evaluate cytotoxic effects after short-term (5 to 48 h) treatments with different MGO concentrations, including low levels, taking into consideration several biochemical endpoints.

In MGO-treated neurospheroids, reduced cell growth proliferation and decreased cell viability occurred early from 5–10 μM , and their compactness diminished starting from 100 μM , apparently without affecting spheroid size. MGO markedly caused loss of the neuronal markers MAP-2 and NSE from 10–50 μM , decreased the detoxifying Glo1 enzyme from 50 μM , and activated NF- κB by nuclear translocation.

The cytochemical evaluation of the 3D sections showed the presence of necrotic cells with loss of nuclei. Apoptotic cells were observed from 50 μM MGO after 48 h, and from 100 μM after 24 h. MGO (50–10 μM) also induced modifications of the cell–cell and cell–ECM interactions. These effects worsened at the higher concentrations (300–500 μM).

In 3D neuronal spheroids, MGO tested concentrations comparable to human samples levels measured in MGO-associated diseases, altered neuronal key signalling endpoints relevant for the pathogenesis of neurodegenerative diseases and aging. The findings also demonstrated that the use of 3D neuronal spheroids of human origin can be useful in a strategy *in vitro* for testing MGO and other dicarbonyls evaluation.

1. Introduction

Methylglyoxal (MGO) is an unavoidably by-product of glycolysis and the major cell-permeant precursor and reactive dicarbonyl intermediate of advanced glycation end-products (AGEs). AGEs are harmful heterogeneous molecules of irreversible products derived from nonenzymatic glycation (spontaneous process) occurring between the reactive carbonyl group of a reducing sugar and nucleic acids, lipids, or proteins (Allaman et al., 2015; Rungratanawanich et al., 2021). Under normal

conditions, cells are not affected by MGO, and the glyoxalase (Glo) system is the most pivotal signal pathway for the detoxication of this substance. Abnormal accumulation of MGO and other reactive α -oxaldehyde dicarbonyl metabolites lead to a dysfunctional state namely *dicarbonyl stress* leading to increased modification of protein and DNA contributing to cell and tissue alteration in ageing and several diseases (Nigro et al., 2017; Rabbani et al., 2016, 2020).

The main drivers of *dicarbonyl stress* are increased formation of MGO, by glycolytic overload and/or decreased MGO metabolism by

* Corresponding author.

E-mail addresses: teresa.coccini@icsmaugeri.it (T. Coccini), francesca.caloni@unimi.it (F. Caloni), luciana.russo@icsmaugeri.it (L.A. Russo), laura.villani@icsmaugeri.it (L. Villani), uliana.desimone@icsmaugeri.it (U. De Simone).

<https://doi.org/10.1016/j.crttox.2024.100176>

Received 13 December 2023; Received in revised form 27 March 2024; Accepted 5 June 2024

Available online 9 June 2024

2666-027X/© 2024 The Authors. Published by Elsevier B.V. This is an open access article under the CC BY-NC-ND license (<http://creativecommons.org/licenses/by-nc-nd/4.0/>).

downregulation of the glyoxalase 1 (Glo1), leading to an excess accumulation of AGEs in tissues including the brain over time (Kuhla et al., 2005; Xue et al., 2011).

AGEs are associated with a variety of pathophysiological mechanisms, such as ageing, diabetes complications, neural apoptosis and neuro-disorders. The deposition of AGEs determines the corresponding tissue damage and dysfunction of repair function, causing serious damage to body tissues and organs (Xu et al., 2023). The formation of AGEs on biological macromolecules alters their structural and functional properties. This type of slow, progressive modification on biologically relevant macromolecules and the accumulation of these modified macromolecules *in vivo* has been implicated in a number of pathologic abnormalities, most prominently the complications associated with normal aging and long-term diabetes. Also, *dicarbonyl stress*, leading to the excess accumulation of AGEs, can be an important mechanistic pathway underlying neurodegeneration and cognitive decline in elderly people (Srikanth et al., 2013; Angeloni et al., 2014; Derk et al., 2018; Lai et al., 2022). In particular, MGO is recognized to be involved in several diseases (Yang et al., 2022) and induction of mitochondrial injury in the central nervous system (CNS) with higher glycation of mitochondrial proteins, associated with an increased production of ROS and proteome damage (Rabbani and Thornalley, 2008; Miyazawa et al., 2010).

Neurons are particularly susceptible to oxidative stress due to their lack of capacity to prevent oxidation and maintain energy under steady internal conditions (Allaman et al., 2015; Yang et al., 2022).

MGO accumulation is detrimental because this metabolic substance is a potent glycating agent in cells, through its reaction with lipids, nucleic acids, lysine proteins, and arginine residues to produce AGEs.

Our recent *in vitro* research studies, applying human neurons cultured in two-dimensional (2D), demonstrated MGO-induced cytotoxicity at low concentrations (Coccini et al., 2023) approaching pathological plasma range determined in several diseases/patients (McLellan et al., 1994; Kong et al., 2014; Piazza et al., 2021). The toxicological effects (i.e. reduction of growth proliferation, overproduction of intracellular ROS, induction of apoptosis, cell death, and neuronal markers reduction) observed in these cells differentiated from primary mesenchymal stromal cells (hMSCs), namely human neuron-like cells (hNLCs), were evident from 10 μM , a concentration much lower compared to that detected in other *in vitro* studies applying human neuroblastoma cell lines, like SH-SY5Y, SK-N-SH, SK-N-MC, M17 where the cytotoxic effects occurred from 250 μM up to over 800 μM (Tajes et al., 2014; Haddad et al., 2019; Suh et al., 2022). Even the neuronal level reduction of NSE occurred in high (500 μM) MGO-treated neuroblastoma cells (SK-N-SH) (Haddad et al., 2019), and the decrease number of MAP-2-positive neurons were also determined after addition of 100 μM MGO to primary culture of rat hippocampal neurons, wherein also their dendrites showed markedly retractile and tortuous appearances (Chen et al., 2010; Radu et al., 2012). Furthermore, the recent employment of human induced pluripotent stem cells (hiPSCs)-derived neurons, evidenced neither cell death nor mitochondrial dysfunction at concentrations of MGO up to 200 μM after 24 h (Hara et al., 2021) or even no loss of viability across a 10–1000 μM MGO range (Conti Mazza et al., 2022). Although human iPSCs are the “gold standard” *in vitro* model mostly applied to obtain the brain cortical/neuronal phenotypes (Smirnova and Hartung, 2024), the rare existing studies indicated a low susceptibility of this derived-neuronal model testing MGO (Hara et al., 2021; Conti Mazza et al., 2022). Primary hMSCs, obtained from different human adult and foetal tissues, have also been recently explored in terms of their neuronal differentiation ability reporting their immense potential to form distinct kinds of neuronal cells (Suma and Mohanan, 2015; Singh and Kashyap, 2016; Kim et al., 2019; Zakrzewski et al., 2019; Gupta and Singh, 2022; Choudhary et al., 2024). Given that, the primary hMSCs, derived from the human umbilical cord, differentiated into neuron-like cells (hNLCs) (De Simone et al., 2022) and grown in three-dimensional (3D) culture system to form spheroids, are exposed to MGO in order to investigate the neurotoxic effects induced by MGO.

Remarkably over the past decade, the emerging human *in vitro* 3D cell culture approaches using stem cells from different organs has received widespread attention allowing them to bridge the gap between cell culture and *in vivo* studies. The potential of 3D structures to complement existing model systems and extend basic biomedical research, drug discovery, and predictive toxicological evaluation into a more physiologically relevant human setting, is becoming ever more widely appreciated and pursued (Wang et al., 2017; Jorfi et al., 2018; Kosheleva et al., 2020).

Spheroids are of lower complexity structurally compared to organoids (Smirnova and Hartung, 2024) but they are simple and popular models for drug screening and toxicity evaluation. Spheroids may contain neurons, astrocytes, and endothelial cells to construct a brain mimicking tissue. The mixture of neuronal and endothelial cells can also form the vascular network structures in spheroids (Shima and Makino, 2022). The presence of glia cells (astrocytes and microglia) in spheroids may provide inflammatory response evaluation to injury or chemical insult (Hogberg et al., 2021). Human cell-based multicellular spheroidal blood–brain barrier model can also be expected to provide a useful and highly accessible experimental platform for accelerating various BBB studies (Kitamura et al., 2021). This physiologically-relevant platform can take important steps toward a more complete evaluation of brain physio-pathology.

With the attempt to better model the biology of human cerebral tissue we have shifted from the *in vitro* mono-layer cultured hNLCs towards the implementation and set-up of 3D neurospheroid cultures (free-floating aggregates of neuronal cells) (De Simone et al., 2022). These 3D human stem-cell-derived neuronal (3D-hNLCs) spheroids more accurately recapitulate the *in vivo* tissue-like state, where the tissue-specific architecture, cell morphology, cell-to-cell and cell-to-extracellular matrix (ECM) interactions resemble those of native tissue more closely.

Since high MGO levels can affect neurons susceptibility inducing AGE formation, a risk factor linked to the development of neurodegenerative disorders, throughout oxidative stress induction and loss of protein function, including protein cross-linking (Currais and Maher, 2013), the present study aimed at evaluating the impact of MGO on 3D-hNLC spheroids treated at day 4 (T4), from seeding in non-adherent ultra-low attachment (ULA) round bottom plates. The effects of different MGO concentrations, including low levels, were assessed after 24 (T5) and 48 (T6) h treatment taking into consideration several MGO-targeted endpoints. Considering that cell adhesion and the ECM are fundamental to the normal structure and function of the three-dimensional tissue spheroids, the effect of MGO on the integrity of cell–cell interactions was assessed through (i) E-cadherin (E-Cad), a transmembrane glycoprotein adhesion molecule that is necessary to form spheroids (Smyrek et al., 2019), as well as (ii) fibrous collagen, one of the major structural components of the ECM besides to be one major target for MGO and AGEs (Nass et al., 2007; Fessel et al., 2014). The internal spheroid structure, evidenced by haematoxylin and eosin (H&E) staining, was analysed and monitored during time. Spheroid growth, size and morphology, cell proliferation and viability, as well as mature neural markers β -Tubulin III (TuJ1), microtubule associated protein 2 (MAP-2), neuron specific enolase (NSE) as indicators of the functional state of nerve cells in normal conditions and pathology were also assessed.

The NF- κ B (Nuclear Factor kappaB – nuclear factor kappa light chain enhancer of activated B cells), one of the most important cell signalling in mediating cellular responses (Kaltschmidt and Kaltschmidt, 2009), and known to play a crucial role in neuroprotection and associated diseases like Alzheimer’s disease (AD) and Parkinson’s disease (PD) (Kaltschmidt et al., 2022), together with the expression of Glo1, the main and limiting enzyme involved in the removal of tissue AGE precursors (i.e. MGO), were evaluated.

2. Materials and methods

2.1. Cell culture media and supplies

Mesenchymal stem cell growth medium 2 (Ready-to-use; PromoCell, Heidelberg, Germany), mesenchymal stem cell neurogenic differentiation medium (Ready-to-use; PromoCell), human fibronectin solution (1 mg/ml; PromoCell), all cell culture reagents, were purchased from Carlo Erba Reagents (Carlo Erba Reagents S.r.l., Cornaredo, Italy). ULA 96-well round-bottomed plates (Corning, Schnellendorf, Bavaria, Germany), 75 cm² tissue culture flasks with vented filter caps (Corning) and glass slides coated with silane (Sigma-Aldrich) were acquired from Merck Life Science S.r.l. (Milan, Italy). Accutase solution (DUTSCHER) was obtained from BioSigma S.p.A. (Cona, Italy).

2.2 Chemicals and Reagents

Methylglyoxal (MGO) solution (40 % in H₂O, Sigma-Aldrich), Bouin's solution, the trichrome stain (Masson) kit, Neo-Mount (Merck) and Fluoroshield (Sigma-Aldrich) mount were purchased from Merck Life Science S.r.l. Trypan blue (TB) solution (0.4 %, Corning) was obtained from VWR International S.r.l. (Milan, Italy). RealTime-Glo™ MT cell viability Assay were acquired from Promega Italia S.r.l. (Milan, Italy). Harris haematoxylin, the eosin Y-solution (0.5 %), the alcoholic solution, and the bio clear solution were purchased from Bio-Optica Milan S.p.A. (Milan, Italy). Primary antibodies (Santa Cruz Biotechnology) conjugated to Alexa-Fluor® 594 or 488 for NSE, NF-κB p50 (D-6), Glo1, and E-Cad were purchased from D.B.A. Italia S.r.l (Segrate, Italy). Primary antibodies (Merck) conjugated to Alexa-Fluor® 488 for MAP-2 and TuJ1 were obtained from Merck Life Science S.r.l.. Hoechst 33258 (Invitrogen) and NFκB p65 (Total/Phospho) Human InstantOne ELISA assay Kit were purchased from Life Technologies Italia (Monza, Italy).

2.3 3D cell culture of human Neuron-Like cells (3D-hNLCs)

Human neuronal cells were obtained from transdifferentiation of the mesenchymal stem cells (hMSCs) derived from human umbilical cord lining membranes isolated and characterized as described by Coccini et al., (2019,2022).

hMSCs at passage (P) 3–4 were cultured (4x10³ cells/cm²) in mesenchymal stem cell growth medium 2 under standard 2D culture conditions (37 °C in a humidified atmosphere of 95 % air/5% CO₂) in 75 cm² flasks. hMSCs were harvested from culture flasks with Accutase solution, according to the logarithmic growth phase, then the neurogenic differentiation medium (ready-to-use) was added to terminate the

digestion. hMSCs were re-seeded at a cell density of 25x10³ cells/200 μl/well in ULA 96-well round-bottomed plates (pre-coated with human fibronectin 10 μg/ml) in mesenchymal stem cell neurogenic differentiation medium (Fig. 1). The non-adherent ultra-low attachment (ULA) round bottom plates allowed formation of a single, highly-reproducible 3D spheroid in each well since these plates have a covalently-bound hydrogel layer to effectively inhibit cellular attachment, thus promoting the spontaneous formation of 3D spheroids (Roper et al., 2021). The latter occurred through intrinsic cell self-organization and adhesion processes, in each well/microcavity after 2 days of culturing. Half of the medium was replaced every 48 h up to 4 days when the spheroids were well formed and tight aggregated. These sphere-like clusters were then used at day 4 (T4) from plating for the MGO treatment. The optimal cell seeding density condition have been optimized, as described in a previous study (De Simone et al., 2022), and arranged to produce spheroids homogenous in size and morphology (a tight spheroid) without a necrotic core, as well as maintain continuous growth for at least six days in culture (the minimum length of time to perform downstream experiments).

Spheroid sizes between 100 and 500 μm have been commonly accepted to be representative of healthy spheroid structures, owing to sufficient oxygen and nutrition transport (Ulusoy et al., 2016). Specifically, small spheroids (<100 μm) might fail to display the complexity of real tissues with low growth rates, whereas large spheroids (>500 μm) might have pronounced necrotic cores due to the diffusion limitations for oxygen and nutrition. Based on these characteristics and the previously established set-up conditions in our lab, 3D-hNLC spheroids were used no later than day 6 from plating.

2.4 Neurospheroid treatment with MGO: Different concentrations at different time points (up to 48 h)

On day 4, the 3D-hNLC spheroids were treated (single dose) with different MGO concentrations (0, 5, 10, 25, 50, 100, 200, 300, 400, 500 μM) up to 48 h, under normothermic (37 °C) conditions in a humidified atmosphere of 95 % air/5% CO₂. Fresh solutions of MGO were prepared immediately before use by diluting MGO stock solution in mesenchymal stem cell neurogenic differentiation medium.

2.5 Cytotoxicity assays: Morphology/size – Trypan blue (TB) staining – Cell growth

Neuronal cell injury was evaluated considering different parameters such as: spheroids morphology and size using phase contrast microscopy, membrane integrity by Trypan Blue staining and cell viability over time by RealTime-Glo™ MT cell viability assay.

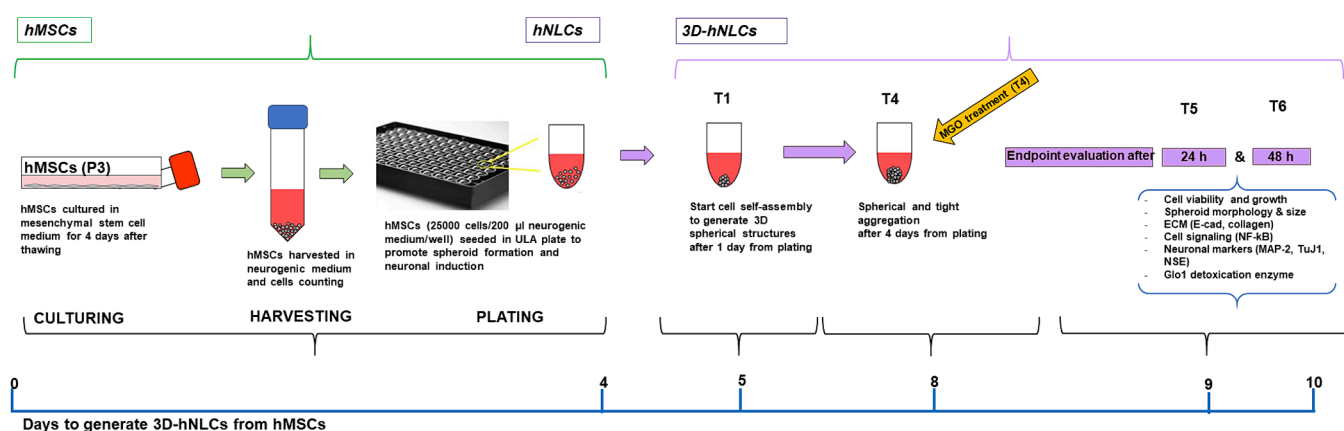


Fig. 1. Schematic representation depicting the protocol to generate the 3D-hNLC spheroids from hMSCs, using ultra-low-attachment round-bottom plates, and their application to assess MGO toxicity. hMSCs were seeded at 25,000 cells/well in ULA plate, that allowed to form 1 hNLC spheroid/well (representing 1 replicate). hNLC spheroids were cultured up to 4 days before MGO treatments.

2.5.1 Spheroid morphology/size by phase-contrast microscopy

3D-hNLC spheroids were observed under inverted microscopy in the bright field mode after MGO (5–500 μM) exposure for 5, 24 and 48 h to evaluate the spheroid health growth/size and the morphological changes. Bright field images of living whole spheroid were recorded at magnification 10X objective, the size was measured directly in the ULA round bottom plates using ImageJ software 1.51 (NIH, Bethesda, MD, USA): a calibration slide was used to calculate the size, and then the pictures ($n = 6\text{--}8$ for each condition) derived from each treatment (5–500 μM) and time point (5, 24 and 48 h) were analysed. Specifically, the bright field images were analysed with the “Measure tool.” Data analysis was performed in Microsoft Excel. We assumed that all spheroids have a round shape, and therefore, the diameter of the spheroids was determined from their area. Digital photographs were captured with a camera (Canon powershot G8) and stored on a PC.

2.5.2 TB Exclusion test

Trypan Blue exclusion test is used to test the cell membrane integrity, based on the principle that live cells prevent the dye penetration, such as trypan blue, since they possess the membrane integrity whereas dead cells do not.

At the end of the different treatment with MGO (5–500 μM for 24 and 48 h), the culture media were carefully aspirated, and the neuro-spheroids were washed with phosphate-buffered saline (PBS; 200 μl /well), and dissociated with Accutase solution (200 μl /well up to 30 min at room temperature (r.t.)). At the end, the enzymatic reaction was inactivated with the neurogenic medium (reaching a final volume of 1 ml). The spheroid disaggregation was obtained by carefully pipetting up and down. Single cell suspension was then mixed with a 0.4 % trypan blue solution (in a ratio of 1:10). A Bürker chamber was used to count manually and determine cell viability. The number of viable cells was determined under light microscopy as a percentage of untreated control cells.

2.5.3 RealTime-Glo™ MT cell viability assay

To monitor the cell responses to MGO, the cell viability was evaluated in 3D-hNLC spheroids over time (1, 7, 24, and 48 h) in the same well after the treatments with concentrations ranging from 5 to 500 μM , according to the protocol supplied by the manufacturer. Specifically, NanoLuc® luciferase enzyme and a cell-permeant pro-substrate (MT Cell Viability substrate), were added directly to the medium in the cells in culture as a reagent. The pro-substrate is not a substrate for luciferase. Viable cells, with an active metabolism, reduce the pro-substrate into a substrate which diffuses into the culture medium where it is used by NanoLuc® luciferase to produce a luminescent signal. The signal correlates with the number of viable cells. Dead cells do not reduce the pro-substrate and produce no signal.

The luminescence was read from 1 to 48 h by a Fluoroskan microplate fluorometer (Thermo Scientific, Milan, Italy) combined with PC (software: Ascent Software, version 2.6). Luminescence is proportional to viable cell number.

2.6 Frozen sections of neuronal spheroids for histochemistry and immunofluorescence analyses

The culture medium was carefully removed from wells containing 3D-hNLC spheroids (untreated and MGO-treated for 24 and 48 h). The 3D-hNLC spheroids, from about 24–32 wells, per condition, were harvested in a microcentrifuge tube, washed with PBS (1 ml/tube), fixed in a 4 % paraformaldehyde solution (PF; for 60 min at r.t.) and re-washed. Then, the spheroids were cryoprotected: they were submerged in 10 % sucrose in PBS solution for 30 min at r.t., then centrifuged, re-submerged in a 20 % sucrose solution for another 30 min at r.t., and finally, submerged in a 30 % sucrose solution overnight at +4 °C. The next day, the spheroids were centrifuged and embedded in an optimal cutting temperature compound (OCT). Four μm -thick cryostatic sections were cut

by using a cryostat (Leica CM 1950, Leica Microsystems, GmbH, Wetzlar, Germany) and deposited on silane prep slides for the subsequent staining and labelling processes or stored at –80 °C. The haematoxylin and eosin stain (H&E) and Masson’s trichrome stain were used to assess the basic tissue structure of the neurospheroids and immunofluorescence staining was performed to evaluate the protein/neuronal marker expression patterns.

2.7 H&E staining

The spheroid sections for each condition and exposure time (24 and 48 h) were processed using histology-staining instruments (Leica ST5020, Leica Microsystems, GmbH, Wetzlar, Germany). Firstly, the spheroid sections were allowed to air dry (2 min at r.t.), then rinsed with tap water (2 min) and stained with Harris haematoxylin (3 min), and again rinsed with tap water (3 min). Afterwards, the sections were covered with a 0.5 % alcoholic eosin Y solution (2 min) and dehydrated in a 95 % alcoholic solution (90 s), in a 100 % alcoholic solution (30 s, twice), and finally in a bio clear solution (clearing agent) (90 s, twice), then were mounted with Neo-Mount. The images were acquired using a light microscope (Carl Zeiss AXIOSKOP 40/40FL microscope, Milan, Italy) equipped with an objective (20X) lens and a digital camera (AxioCam MRc5 Carl Zeiss, Milan, Italy) and stored on PC.

Quantification of apoptotic cells was performed, on 3D-spheroid sections, counting them in $n = 8\text{--}10$ pictures for each concentration and each time point. Data were expressed as mean \pm S.D. (Standard Deviation).

2.8 Masson’s trichrome staining

The use of Masson’s trichrome staining of tissue sections is a method for detection of morphological alterations indicative of a fibrotic phenotype. This method detects the extent of collagen fibres deposition and, because it employs the combination of three dyes, can simultaneously identify nuclei (dark-purple stain) using Weigert’s iron haematoxylin, cytoplasm (scarlet stain) by the “Biebrich scarlet-acid fuchsin solution”, and the collagen type I fibres (blue stain) by Aniline blue.

The sections obtained from MGO-treated spheroids were stained with Masson’s trichrome kit by following the producers’ instructions. The 3D-hNLC spheroid sections were first left to equilibrate at r.t. (10 min), then were rehydrated in deionized water (10 min at r.t.). The sections were covered with Bouin’s solution (pre-warmed at 56 °C) for 15 min, then were cooled in tap water and washed (three times; 5 min for each washing) to remove the yellow color from the sections. The slides were stained (5 min) using working Weigert’s iron haematoxylin solution (Part A plus Part B), washed again in tap water (three times; 5 min for each washing), and rinsed using deionized water (three times; 5 min for each washing). Then, they were stained using the Biebrich scarlet-acid fuchsin solution (5 min), and after the washing (three times in deionized water; 5 min for each washing), the sections were stained in a working phosphotungstic/phosphomolybdic acid solution (5 min), then in an aniline blue solution (5 min), and then in a 1 % acetic acid solution (2 min). Finally, the sections were rinsed in deionized water (three times; 5 min for each washing), dehydrated through an alcohol scale (80 %, 90 %, 100 %), and cleared in 50 %:50 % alcohol:xylene, and then in 100 % xylene. The sections were then mounted with Neo-Mount. Images were acquired in the brightfield (20X magnification; Zeiss AXIOSKOP 40/40FL microscope) and stored on PC.

The collagen positive fibres (blue colour component) were quantified by the ImageJ software applying the protocol from [Chen et al. \(2017\)](#). Specifically, the images with Masson’s trichrome stain were processed using the “Colour Deconvolution” plugin. Five fields from each image (spheroid) were captured. $N = 5$ spheroids for each concentration at each time point were considered. Data were expressed as mean \pm S.D..

2.9 Expression of *Glo1*, neuronal markers, *NF-κB* (p50), and *e-Cad* by immunofluorescence analyses

The expressions of the *Glo1*, different neuronal markers (*MAP-2*, *NSE* and *TuJ1*), *NF-κB* (p50) and *E-Cad* were evaluated after 24 and 48 h MGO treatment (10–500 μM) by immunofluorescence analyses. After rehydration, the cryo-sections of the 3D-hNLC spheroids were permeabilized (with 0.25 % Triton X-100 in PBS solution for 10 min at r.t.) and incubated for 30 min in a blocking buffer (1 % bovine serum albumin (BSA) in PBS). Afterward, the spheroids were incubated with primary antibodies conjugated to Alexa-Fluor® 488 (green colour) or Alexa-Fluor® 594 (red colour) against: *Glo1*, *MAP-2*, *NSE*, *TuJ1* (diluted 1:100, in 1 % BSA solution), and *NF-κB* p50 (D-6) and *E-Cad* (diluted 1:50, in 1 % BSA solution) for 60 min at r.t. in the dark. Next, the spheroid sections were washed with PBS (three times; 5 min for each washing) and the nuclei were detected using Hoechst 33258 (blue colour) (5 μM for 10 min at r.t.) for all endpoints except *NF-κB*. After washing the sections were finally mounted with Fluoroshield. The fluorescence images were acquired using a CX41 Olympus fluorescence microscope (Olympus, Segrate, Italy), with the excitation light being provided by an EPI LED Cassette and combined with a digital camera (Infinity2). The measurement conditions were the following: 470 nm excitation (T% = 40), 505 nm dichroic beamsplitter, and 510 nm-long pass filter. The fluorescence images for *NF-κB* were captured using Zeiss microscope (AXIOSKOP 40/40FL) equipped with a digital camera (AxioCam MRC5, Zeiss) and mercury vapor short-arc lamp, excitation filter: 546 nm; emission filter: 567 nm, and combined with a digital camera (AxioCam MRC5). Digital images of the 5–8 randomly selected microscopic fields were captured using a 20X objective lens.

2.10 Evaluation of *NF-κB* (p65) by ELISA assay

NF-κB 65 phosphorylation in 3D-hNLCs was evaluated after MGO exposure (10–500 μM) by a sandwich ELISA, following the manufacturer's instructions. Briefly, after each exposure time point, the culture medium was carefully removed from each well and the hNLC spheroids were washed with PBS (200 μl/well). A single cell suspension was obtained using Accutase solution (200 μl/well, for 30 min). A least 24–32 spheroids per condition were pooled. The cells, counted using the Fast Read 102® counting chamber to estimate viable cell number, were normalized for the same cell number (99000 cells) per each condition. Then, the pellet samples were lysed and in each well, 50 μl of cell lysate samples (control and treated MGO groups), cell lysis buffer 1X (negative control), and positive control (*NF-κB* p65) were individually pipetted into the pre-coated ELISA plate, and finally the antibody cocktail added to each well. Plate was incubated for 1 h with shaking at 300 rpm at r.t. and thereafter washed (three times with washing buffer 1X, 200 μl/well) before adding a detection reagent for 30 min with shaking at 300 rpm at r.t., sequentially, the detection reaction was stopped using stop solution (100 μl/well). The optical density (O.D.) was immediately measured at 450 nm using a microspectrophotometer (BioRad, Benchmark, Segrate, Italy). Each sample was run in duplicate. Data were expressed as the percentage of control group and as a mean ± S.D..

2.11 Data analyses

Data of the cytotoxicity effects (TB, cell growth, spheroid diameter) were expressed as the mean ± S.E. (Standard Error) of three separate experiments each carried out in four (TB test) or eight replicates (cell growth). Fluorescence intensity (FI) quantification was performed by digital image processing (n = 5–8 images, for each MGO concentration tested for each timepoint) using ImageJ software. FI data of *E-Cad*, neuronal markers, and *Glo-1* were expressed as RLU (Relative Light Unit) mean ± S.D..

Statistical analysis was performed by one-way ANOVA followed by post-hoc Tukey test for multiple comparisons. P values less than 0.05

were considered to be significant.

The IC₅₀s (50 % Inhibitory Concentration) for MGO were calculated from cell viability curves obtained from TB data. IC₅₀ determination was performed using AAT Bioquest IC₅₀ calculator available on <https://www.aatbio.com/tools/ic50-calculator>.

3. Results

3.1 Morphological and size analyses of 3D-hNLC spheroids by phase-contrast microscopy imaging after MGO exposure

At Day 4 (after seeding and induction of hMSCs to transdifferentiate in human neuron-like cells), the 3D-hNLC spheroids were well formed and tight aggregated, thus having reached their optimal size on day 4, 3D spheroids were then suitable to be used in several functional assays.

In details, cells spontaneously formed 3D spheroids, in each well, 4 days after plating (25x10³ cells/200 μl/well) in ULA 96-well round-bottomed plates containing mesenchymal stem cell neurogenic differentiation medium.

The Fig. 2A shows the growth of 3D-hNLC spheroids in term of shape and diameter size from cell seeding. During the early assembly phase (2 h) the hNLCs appeared as cell loose aggregate forming a flat layer of cells at the bottom of the well. At 6 h, hNLC structures started to form aggregates showing irregular and jagged boundaries due to the progressive cellular integration after seeding. After 24 h, hNLC spheroid boundaries were more defined and during culture, from day 2 to day 4, the spheroids appeared well defined and tight aggregated (Fig. 2A). Notably, 3D-hNLCs were self-assembled into a round single spheroid per well.

3D-hNLC spheroid formation typically occurred by the 2nd day (at this point, the cells were aggregated) and the spheroids became tight, compact, and rounder by the 4th day (Fig. 2A). The spherical shape was maintained throughout the culture process until day 6.

Day 4, when the diameter of the spheroids measured 471.74 ± 10.62 μm, was selected for starting the treatments with MGO at different concentrations (from 5 to 500 μM) and the effects were evaluated after 24 and 48 h of treatment (i.e., at day 5 (T5) and 6 (T6)). Morphological and size evaluation were also estimated at an earlier time point (i.e., 5 h).

MGO treatments caused concentration- and time-dependent morphological alterations to the structure of spheroids as observed by phase-contrast microscopy (Fig. 2B). Compactness decreased in association with an increase cell detachment from the main body (peripherally dispersed) that was visible at 300 μM after 5 h, ≥ 200 μM after 24 h, and ≥ 100 μM after 48 h. Whereas, the spheroids maintained a quite regular shapes when compared to control (Fig. 2B). The spheroid assembly is apparently maintained throughout the experimental condition.

No change in spheroid area was observed within the given treatment concentrations and times (Fig. 2C).

3.2 Effects of MGO on cell viability and growth

3.2.1 TB Evaluation

TB exclusion test evaluation indicated that the cell viability of the 3D-hNLC spheroids was affected by MGO treatments. An increase of dead cells (~10 %) compared to control was evident starting from 100 μM after 24 h reaching a maximum effect (cell death: ~ 20–40 %) at the higher concentrations tested (200–500 μM) (Fig. 3A). Similar trend of cell mortality also persisted after 48 h MGO treatments, with, remarkably, reduction of viable cells occurring from lower concentration, i.e., 50 μM (Fig. 3A). The IC₅₀ concentrations were 241.70 μM and 195.66 μM after 24 h and 48 h, respectively.

3.2.2 Cell growth evaluation

Cell growth evaluation was performed to assess the MGO effects on the cell viability in real time and over time (from 1 up to 48 h). Significantly decrease of cell growth was induced already after 1 h

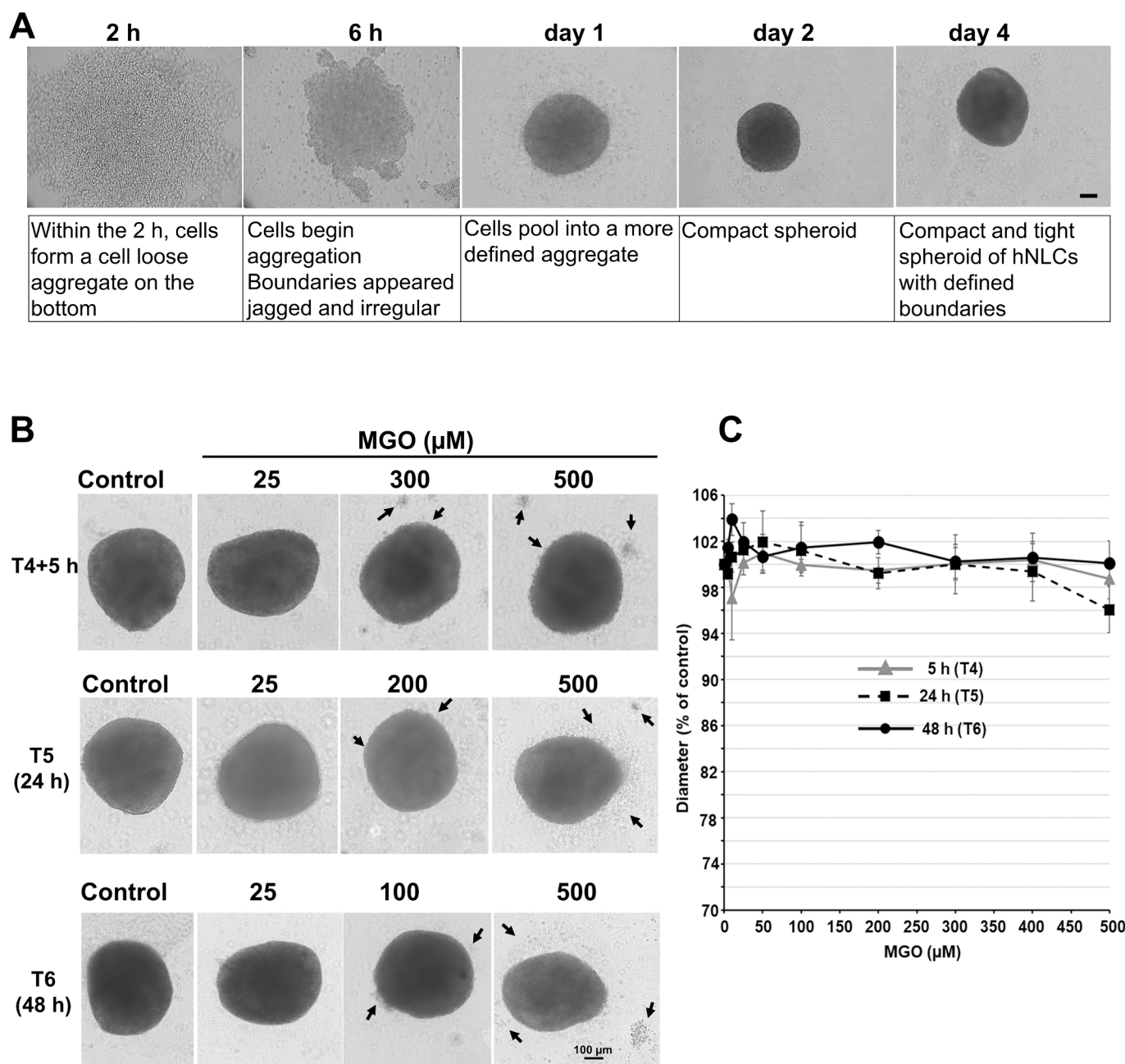


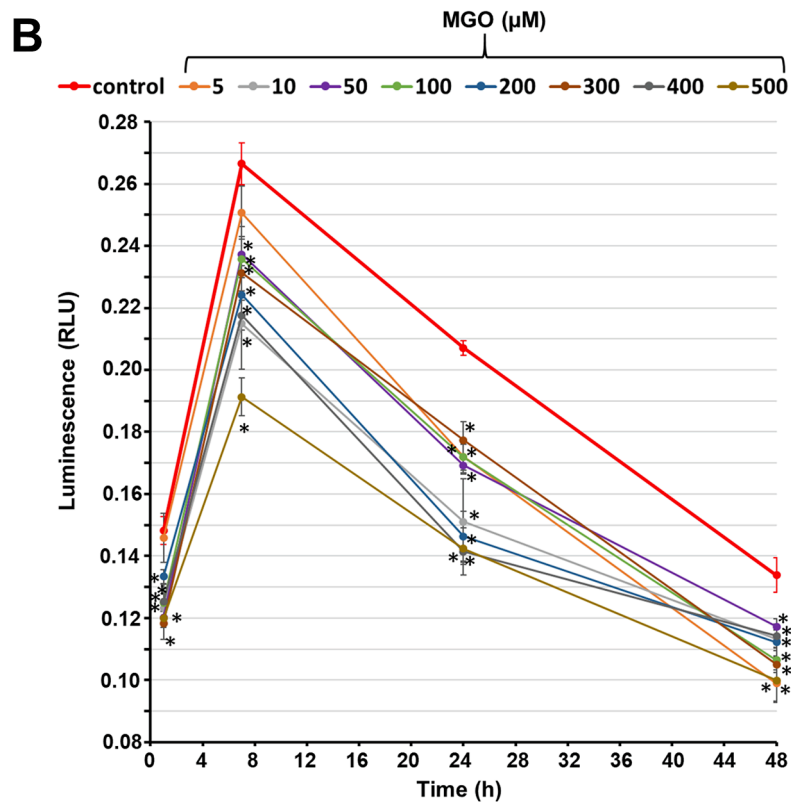
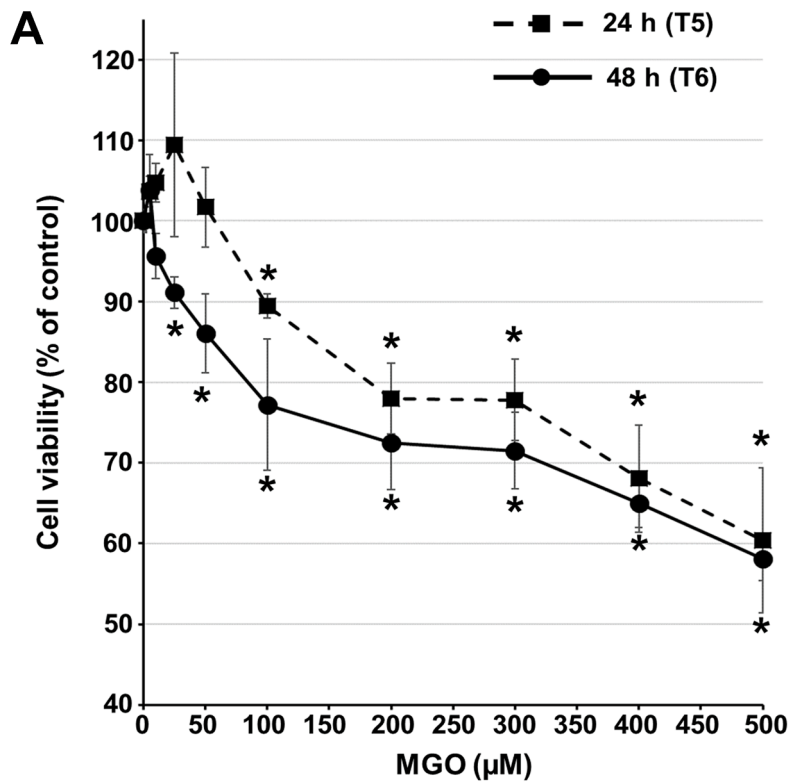
Fig. 2. A) Morphological analysis by phase-contrast microscopy of the 3D-hNLC spheroid formation over a 4-day period in 96-well spheroid microplate. At 2–6 h after seeding, hNLC aggregates had not yet reached a compact spheroid-like structure. Progressively, from day 1 onwards, the cell aggregate structures became more tightly packed, and at day 4 (T4) a complete 3D-hNLC spheroid formation appeared as a dense spherical structure. This time point was chosen as the starting point for MGO treatments. Scale bar: 100 μm . B) Morphological analysis by phase-contrast microscopy of the 3D-hNLC spheroids after MGO treatments. 3D-hNLC spheroids of controls were well formed and tight aggregated. MGO treatments did not cause diameter changes when compared to control samples, but induced a loss of compactness i.e., appearing of detachment of the cells from the main body starting at 300 μM after 5 h (day 4), 200 μM after 24 h (day 5) and 100 μM after 48 h (day 6). Black arrows indicate cells detachment from the main body. Scale bar: 100 μm . The spheroid assembly is apparently maintained throughout the experimental condition. C) Diameter evaluation after MGO exposure. No changes in the spheroid diameter, for each concentration tested (5–500 μM) and time points considered (5–48 h), were observed. 3D-hNLC spheroid diameter was calculated by ImageJ software. Data were normalized to the mean value obtained under control condition and expressed as percentage (% of each control) and plotted as the mean \pm S.E..

exposure to MGO starting at ≥ 10 μM compared to control growth trend. Furthermore, after 24 h and 48 h exposure, a lower concentration (≥ 5 μM) was detrimental and persisted at the higher concentrations (Fig. 3B).

3.3 3D-hNLC spheroids morphology evaluation by H&E and Masson's trichrome stainings

To assess the overall morphological characteristics, structural architecture and extracellular matrix, the spheroids were histologically sectioned and stained with H&E and Masson's Trichrome.

H&E staining showed marked differences between the control and treatment groups. Histological analysis of the spheroid sections of



(caption on next page)

Fig. 3. A) Cell viability evaluation by Trypan blue (TB) exclusion test. 3D-hNLC spheroids were treated at day 4 with increasing concentration of MGO (5–500 μM) for 24 and 48 h. The cell number mean \pm S.D. of controls were at T5: 30433.30 ± 984.59 and at T6: 52250 ± 580.20 , respectively. Data were normalized to the mean value obtained under control condition and expressed as percentage (% of each control) and plotted as the mean \pm S.E.. B) Cell viability over time by RealTime-Glo™ MT cell viability assay. MGO decreased cell growth of 3D-hNLC spheroids in a time- and concentration-dependent manner: the effect started after 1 h treatment at 10 μM MGO, and persisted up to 48 h of exposure. Results are provided as means \pm S.E. of three independent experiments performed in eight replicates. * $p < 0.05$, statistical analysis by one-way ANOVA by Tukey's multiple comparisons test.

control, as shown in Fig. 4, displayed a uniform pattern of cell arrangement through the spheroids, a compact and uniform structure, and a well-defined external perimeter. The sections of 3D-hNLC spheroid control showed nuclei and cytoplasm well contrasted and revealed equally distributed chromatin in the nucleus (basophilic structure stained by haematoxylin) and intact cytoplasm (eosinophilic structure stained by eosin) indicative of viable healthy hNLCs. Notably, no necrotic core or hypoxia, in terms of reduced cell density and apoptotic nuclei, were present in control spheroids, as suggested by absence of pale eosinophilic cytoplasm in the core of spheroid sections.

In the MGO-treated 3D-hNLC spheroids, some dead cell was identified by the evidenced of nuclear condensation (visualized by a more purple haematoxylin staining) and enucleation (stained by pink eosin staining only) starting at 100 μM MGO treatment after 24 h exposure. A lower concentration, such as 50 μM , was detrimental when the exposure was prolonged, i.e. 48 h. Moreover, some cells showed shrinking of cytoplasm (evidenced by absence of eosin stain), and other cells showed karyorrhectic nuclei (dark purple colour intensely stained by haematoxylin) characteristic of the apoptotic cells (Fig. 4). The sections also displayed inter-cellular structural alterations due to loss of cell–cell contacts since the space between cells was pink stained without nuclei (haematoxylin uncoloured). The latter may indicate the presence of either protein fibres laid down in some regions of the hNLC spheroids, since extracellular matrix is an eosinophilic structure (see below ECM staining), or necrotic cells with loss of nuclei (Fig. 4). The effects were worsened at the higher concentrations tested (300–500 μM).

In 3D-hNLC spheroid sections of controls, few apoptotic cells (6.2 ± 1.9 and 7.2 ± 2.4 apoptotic cell number, after 24 and 48 h, respectively) were observed (Fig. 4B and D) for both time points considered. In MGO-treated neurospheroids, the apoptotic cell number increased in a concentration- and time-dependent manner: after 24 h, the effect started at 100 μM (+130 %) reaching a maximum effect at 500 μM (+250 %) (Fig. 4B). Similar apoptotic cell increase was observed after 48 h for 100–500 μM MGO (Fig. 4D).

Notably, no alterations in morphological characteristics and structural architecture were observed at the lowest concentration tested (10 μM) for both time points (Fig. 4).

The Masson's trichrome utilizes three stains to selectively identify: the nuclei purple stained (basophilic structure), the cytoplasm red stained (eosinophilic structure), and the collagen type I fibres blue stained (predominantly present in ECM) that plays a dominant role in maintaining the structural integrity of the spheroids (Fig. 5). Control samples showed nuclei and cytoplasm well contrasted and distinct compartmentalization of the thick dense collagen fibres (intensely blue stained) that surround the single cells indicating the capacity of 3D-hNLCs to form their own ECM.

Notably, the staining pattern of collagen I in images of spheroids showed a significant reduction of the fibrillary collagen evidenced by a lighter blue colour throughout the spheroid following treatment with MGO. Collagen quantification, by ImageJ program, indicated a collagen reduction area of about 70 % (control value of % collagen area: 72.64 ± 2.81 , and 65.65 ± 6.25 at 24 h and 48 h, respectively) starting at 100 μM after 24 h and 50 μM after 48 h, with further exacerbation (85 % decrease) at the higher concentrations (300–500 μM) (Fig. 5).

3.4 E-cadherin expression

The E-cadherin is involved in the regulation of cell adhesion (cell to

cell) and cell-ECM interactions. E-cadherin has also been recognized as one of the key factors involves in tissue organization to maintain the morphological structure and functional integrity of the spheroids derived from different cell types including neurons (Casey et al., 2001; Enmon et al., 2002; Lin et al., 2006; Ivascu and Kubbies, 2007; Saias et al., 2015; Ivanov and Grabowska, 2017; Smyrek et al., 2019; Perez et al., 2023). When cells lose the E-cadherin, they also lose the ability to aggregate as a spheroid. Actually, the expression of the high E-cadherin level correlates with the ability of the cells to form compact spheroids.

Expression of E-Cad in 3D-hNLC spheroids was explored using immunofluorescence analysis. Control samples exhibited cytoplasmatic positivity for E-Cad (green fluorescence). The fluorescence intensity decreased (about 20 %) in treated samples started at 100 μM MGO after 24 h exposure and lasted at the higher concentrations tested (300–500 μM) (Fig. 6). Similar intensity pattern of fluorescence signal was observed after 48 h exposure (data not shown).

3.5 Neuronal markers evaluation

The neuron-like phenotype was confirmed by the expression of the MAP-2 (a mature neuron marker), NSE (cytoplasmic protein expressed by mature neurons), and TuJ1 (a microtubule element of the tubulin family, structural marker predominantly in neurons). Several studies report that human MSCs that differentiate into neuron-like cells exhibit increased characteristics of neuronal protein markers such as MAP-2, NSE, and TuJ1 (Sanchez-Ramos, et al., 2000; Woodbury et al., 2002; Levy et al., 2003). MAP-2, a protein that belongs to the microtubule-associated protein family, is involved in microtubule assembly, and is primarily localized in the dendrites, implicating a role in determining and stabilizing dendritic morphology during neural development. NSE also possesses neurotrophic properties on a wide spectrum of CNS neurons and is needed for neuronal cell survival. Beta tubulins are one of the two structural components that form microtubule network and TuJ1 is specifically localized to neurons. TuJ1's expression correlates with the earliest phases of neuronal differentiation and for this reason it has implications in neurogenesis, axon guidance and maintenance.

The fluorescence intensity of MAP-2- and NSE-positive 3D-hNLCs decreased (about 30–60 %) in a concentration- and time-dependent manner after MGO exposure (Fig. 7). Specifically, decrease of green (MAP-2) staining intensity (about 30 %) was detected from 50 μM after 24 h (Fig. 7A). Following 48 h exposure, the decrease of fluorescence intensity was evidenced at the lowest concentration tested (10 μM) with further exacerbation at the higher concentrations (300–500 μM) (Fig. 7B). Similar pattern was observed for the red NSE-positive 3D-hNLCs (Fig. 7A, B).

Notably, none of the tested MGO concentrations affected the expression of TuJ1 at both time points (FI at 48 h was: 59.85 ± 9.99 and 53.13 ± 8.79 RLU (Relative Light Unit) for the control and 500 μM MGO treatment, respectively) (Fig. 8).

3.6 Glyoxalase-1 expression

Glo1 green fluorescence intensity decreased (about 30 %) starting from 50 μM after 24 h and persisted (about 35 %) at the higher MGO concentrations (300–500 μM) (Fig. 9). Similar trend was observed after 48 h exposure (data not shown).

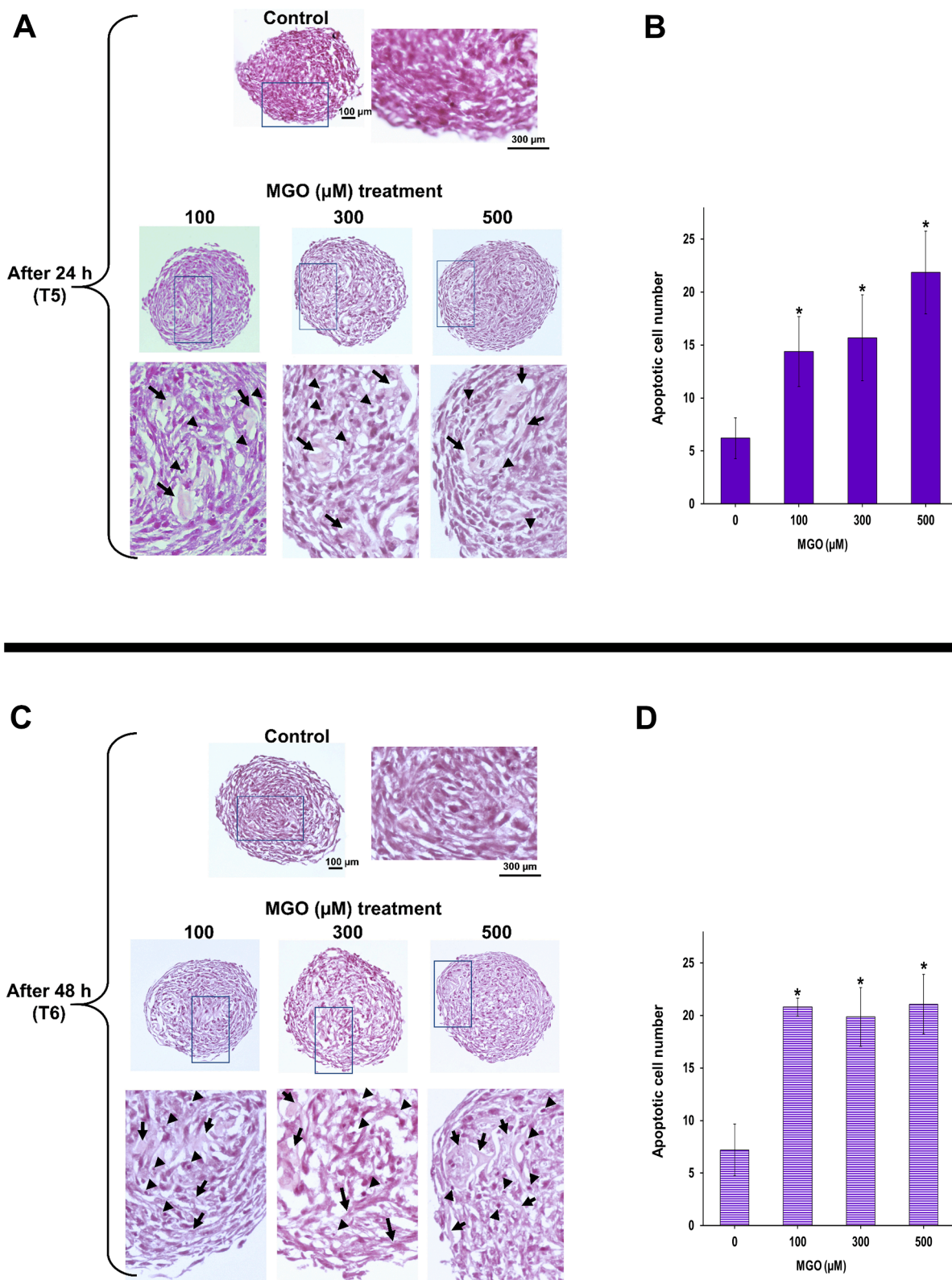


Fig. 4. Spheroid histology by H&E. In the control spheroids, the cells were arranged close together and appeared densely packed, nuclei (basophilic structure stained by haematoxylin) and cytoplasm (eosinophilic structure stained by eosin) well contrasted. No necrotic core was visible how observed by absence of pale eosinophilic cytoplasm in the core of spheroid sections. In MGO-treated spheroids, a loss of cell packing, shrinking of cytoplasm (evidenced by absence of eosin stain), and apoptotic cells (dark purple colour intensely stained by haematoxylin; black head arrows) were observed starting at 100 μM after 24 h (A) and 50 μM after 48 h (C). Pink stained areas (black arrows) with non-appearance of haematoxylin potentially indicated interstitial spaces between individual cells and necrotic areas. Representative images were taken using magnification X20; the rectangle in pictures indicate enlargement of 3X. Quantitative analysis of apoptotic cells after 24 (B) and 48 h (D). Data are provided as means \pm S.D. of $n = 8-10$ H&E section imagines for each concentration and each timepoint. * $p < 0.05$, statistical analysis by one-way ANOVA by Tukey's multiple comparisons test.

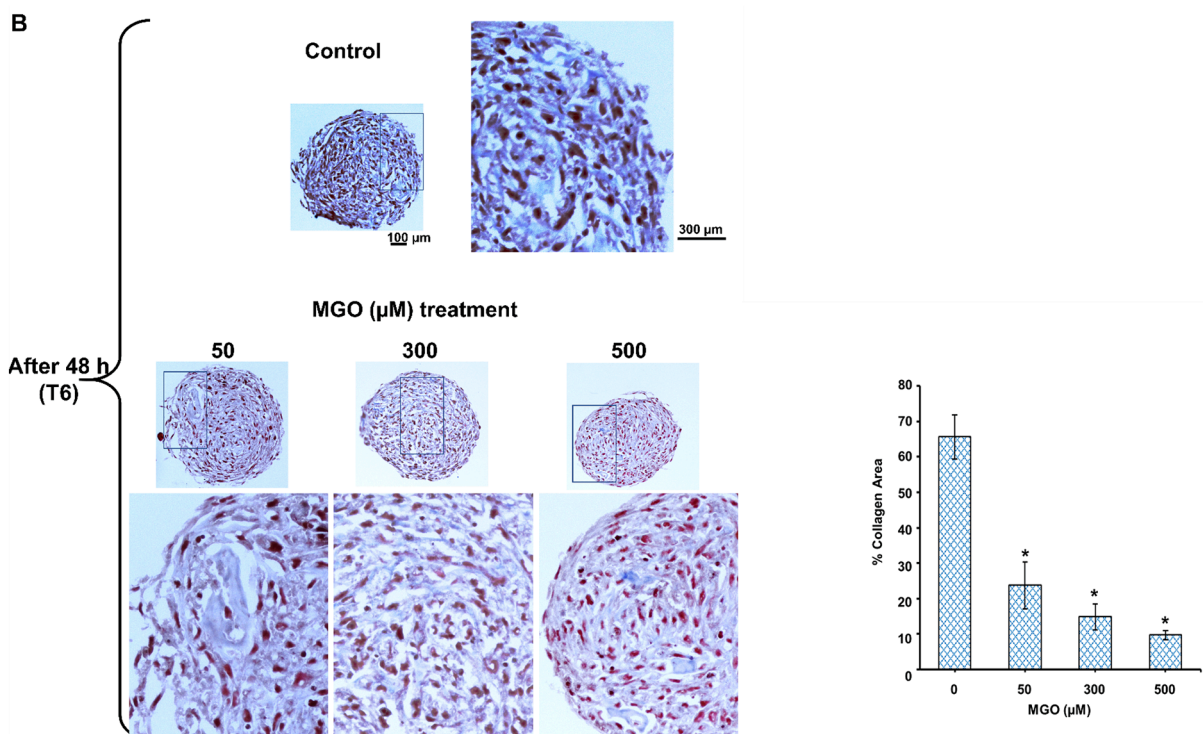
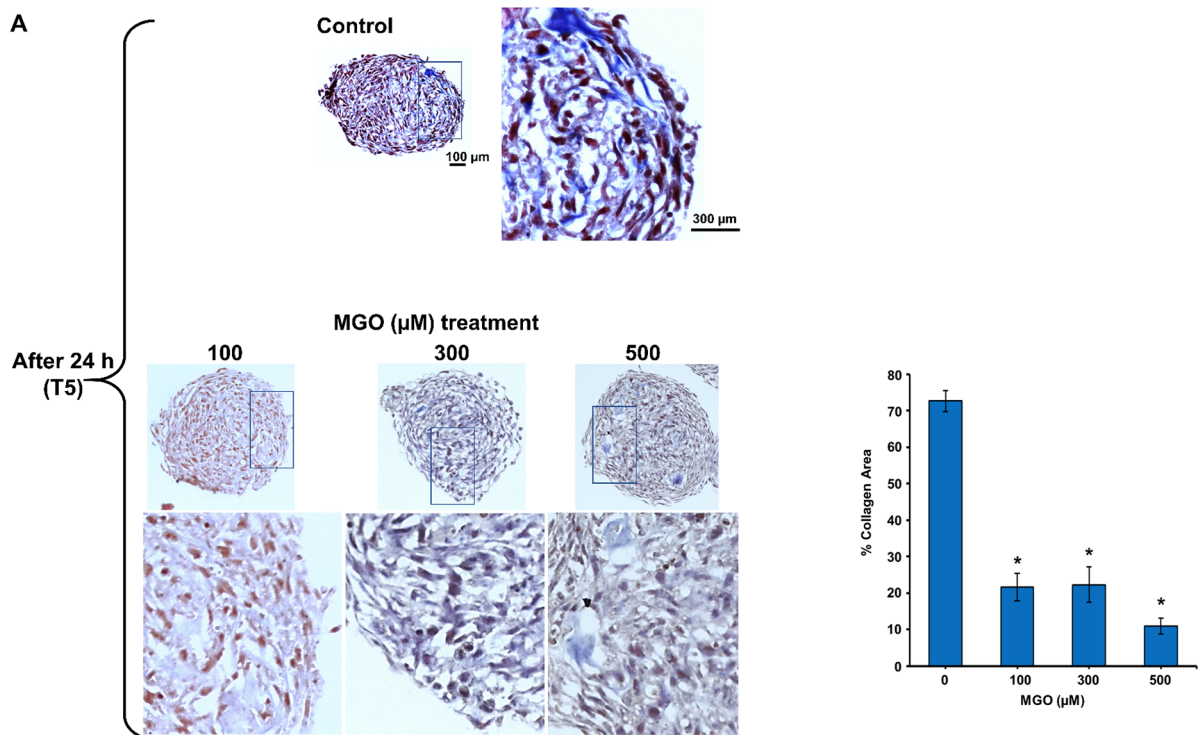


Fig. 5. Masson's trichrome staining to reveal the collagenous extracellular matrix (ECM) as blue colour. Control spheroids showed nuclei (purple coloured) and cytoplasm (red stained) well contrasted. The thick dense collagen fibres (intensely blue stained) were observed outside the single cells. A loss of blue staining, indicating reduction of collagen I, was observed in 3D-hNLC spheroids treated with MGO at 100 μM after 24 h (A) and 50 μM after 48 h (B) and respective collagen quantification, by ImageJ program, was shown. The MGO effects worsened at the higher concentrations tested. Representative images were taken using magnification X20; the rectangle in pictures indicate enlargement of 3X.

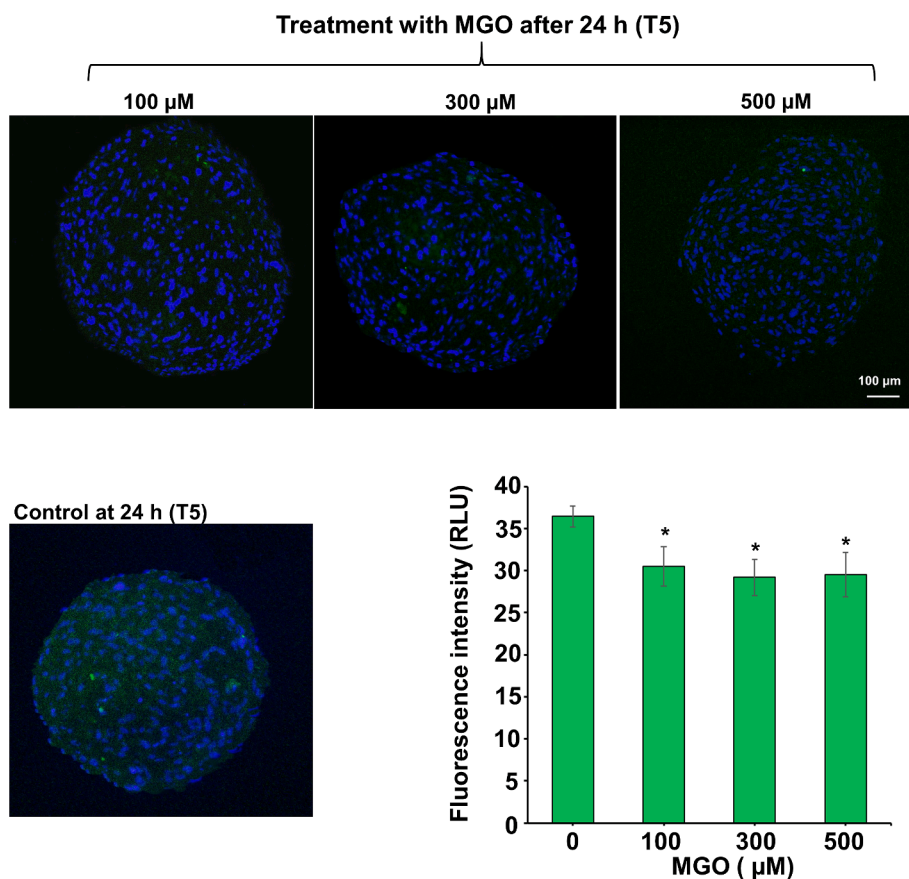


Fig. 6. Immunofluorescence findings using E-cadherin antibody. Representative merged images of E-Cad-positive 3D-hNLCs after 24 h exposure to MGO (100, 300 and 500 μM). Nuclei were stained with Hoechst 33258. Fluorescence microscope images were taken using magnification X20. Bar chart represents the quantitative analysis of fluorescence intensity. Data are expressed as mean \pm S.D.. * $p < 0.05$, different from control, statistical analysis by One-way ANOVA followed by Tukey's post hoc test.

3.7 NF- κB evaluation

MGO has been shown to trigger/activate NF- κB activity in several *in vitro* cellular models including neuroblastoma cells (Wang et al., 2014) as well as to induce a rapid NF- κB translocation from the cytoplasm to the nucleus (Lin et al., 2016). The activation of NF- κB system in the downstream of the AGE/receptor of AGE (RAGE) pathway also down-regulates Glo1 expression (Nigro et al., 2019). Both, MGO-dependent activation of NF- κB (increase) and Glo1 inhibition, contribute to provide the conditions for *dicarbonyl stress* known to be associated with metabolic and age-related diseases. Activation of NF- κB depends on phosphorylation.

NF- κB constitutes a family of transcription factors consisting of five members, including Rel (c-Rel), RelA (p65), RelB, NF κB 1 (p50 and its precursor p105), and NF κB 2 (p52 and its precursor p100). NF- κB dimers, containing p65, are activators of transcription. Upon stimulation, the p65 is phosphorylated and a cleavage of the p105 subunit into its active p50 form occurred. Subsequently, the p50/p65 complex translocates to the nucleus where it activates transcription.

The NF- κB p65 phosphorylation, as indicative of activation, was evaluated by the ELISA assay in MGO-treated 3D-hNLCs. After 24 h exposure, the levels of the phospho-NF- κB p65, increased (+140 %) starting from 10 μM MGO compared to control (control OD value: 0.200 ± 0.02) and remained significantly high (about 50–95 %) between 100 and 500 μM (Fig. 10A). Following 48 h, the phospho-NF- κB p65 remained high (+30–55 %) at the higher concentration tested (300–500 μM), while, at MGO ranging between 10 and 200 μM , the phospho-NF- κB p65 value returned to control level (OD value: 0.243 ± 0.001) (Fig. 10A).

NF- κB activation after MGO exposure was also evidenced by immunofluorescence staining in 3D-hNLCs. The images, of controls and MGO up to 200 μM , exhibited NF- κB p50 cytoplasmic localization as evidenced by a widespread red fluorescence, while nuclei remained unstained (Fig. 10B). Higher MGO concentrations, 300 and 500 μM , caused the activation of the NF- κB pathway as indicated by the increase NF- κB p50 fluorescence intensity in the nuclei. The effect was visible after 24 h and persisted up to 48 h (Fig. 10B).

4. Discussion

The study demonstrates that 3D spheroids of neuron-like cells of human origin, generated from the differentiation of mesenchymal stromal cells derived from human umbilical cord, can be a useful species-specific tool to complement the *in vitro* neurotoxicity testing for the MGO and other dicarbonyls evaluation. Moreover, the present investigation is the first study exploring MGO-induced toxicity by applying a three-dimensional model of human stem cell-derived neurons.

In the applied 3D model of human neurons, MGO was shown to be very reactive reducing cell growth proliferation already after 1 h exposure to 10 μM , and even a lower concentration, such as 5 μM , was deleterious after 24–48 h. MGO, from 50–100 μM , decreased cell viability (Fig. 3), in accordance with the results obtained in the same neuron type though cultivated in 2D monolayer (Coccini et al., 2023). In MGO-treated spheroids the compactness diminished as indicated by an increased cell detachment from the main body (peripherally visible dispersed cells), starting from 100 μM , apparently without affecting the spheroid area size (Fig. 2). The cytochemical evaluation of the 3D

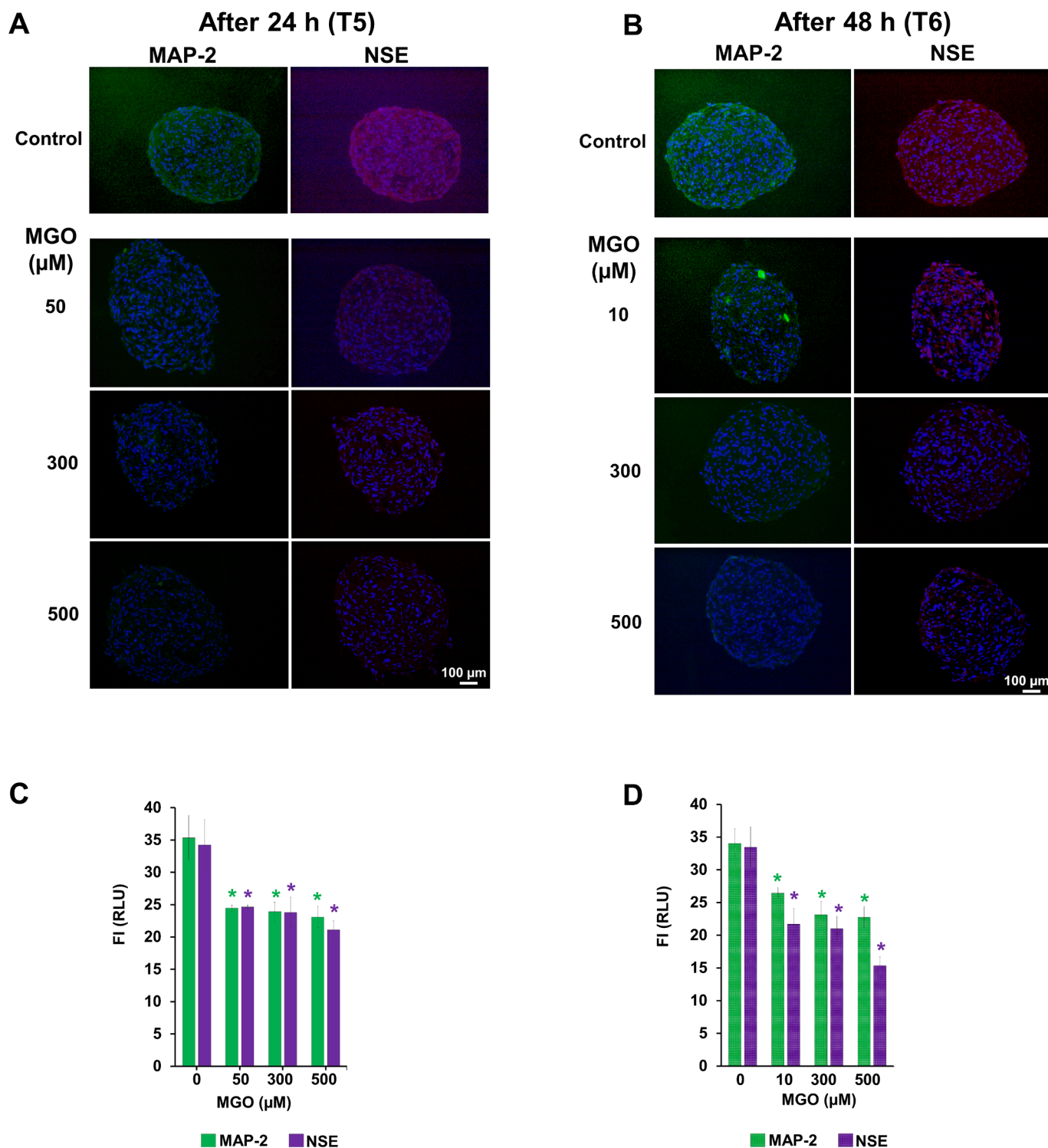


Fig. 7. Immunofluorescence. Representative merged images of MAP-2- and NSE-positive 3D-hNLCs after 24 h (A) and 48 h (B) MGO treatments (10–500 μ M). Nuclei were stained with Hoechst 33258. Fluorescence microscope images were taken using magnification X20. Immunofluorescence quantitative analysis of MAP-2 and NSE after 24 (C) and 48 h (D) exposure to MGO (10–500 μ M). Data represent the mean \pm S.D. * $p < 0.05$ statistical analysis by one-way ANOVA by Tukey’s multiple comparisons test.

sections evidenced some (i) dead cells, proved by nuclear condensation and enucleation, (ii) cells with shrinking of cytoplasm, and (iii) others showing karyorrhectic nuclei characteristic of the apoptotic cells (Fig. 4). In particular, the apoptotic cell number increased in a concentration- and time-dependent manner. After 24 h, the effect started at 100 μ M MGO (+130 %) reaching a maximum effect at 500 μ M (+250 %) (Fig. 4B). Similar apoptotic cell increase was observed after 48 h for

100–500 μ M MGO (Fig. 4D). Sections also displayed inter-cellular structural alterations due to loss of cell–cell contacts as indicated by the pink stained space between cells without nuclei (haematoxylin uncoloured). The alterations worsened at the higher concentrations tested (300–500 μ M).

The evaluation of ECM, revealed collagen content decrease that was MGO concentration- and time-dependent starting at 50 μ M after 48 h or

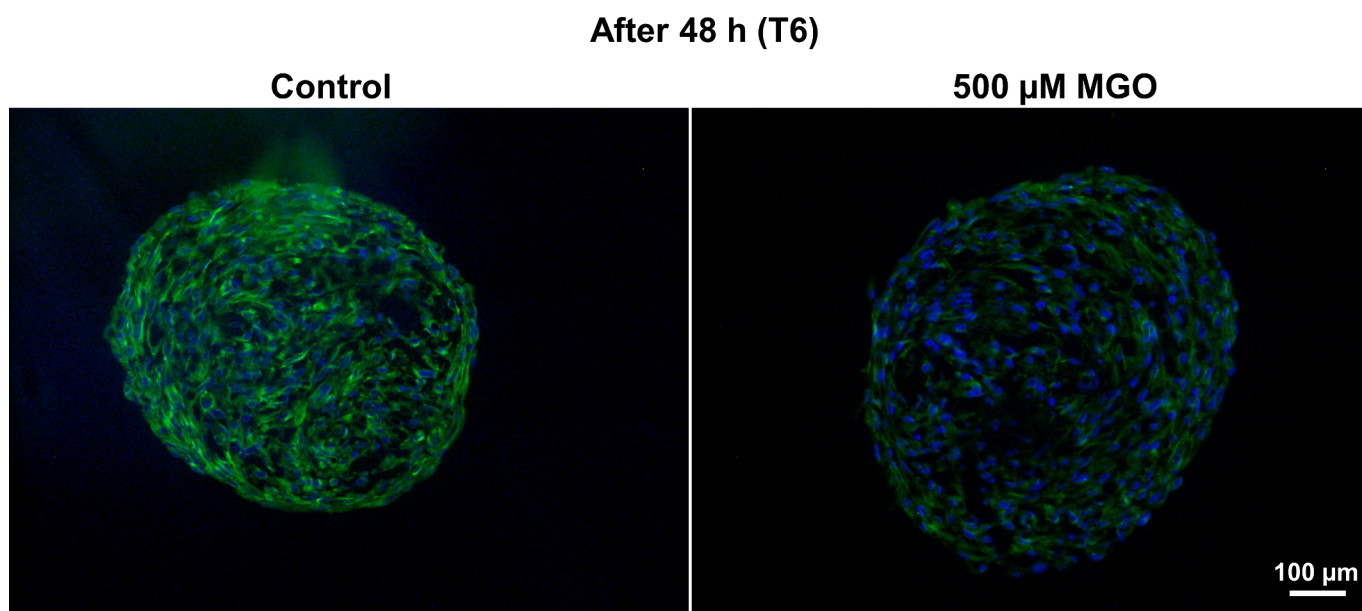


Fig. 8. Immunofluorescence analysis of TuJ1 in 3D-hNLC spheroid sections. Representative image of TuJ1-positive 3D-hNLCs after 48 h exposure to MGO at the highest concentration tested (500 μM). Nuclei were stained with Hoechst 33258. Fluorescence microscope images were taken using magnification X20.

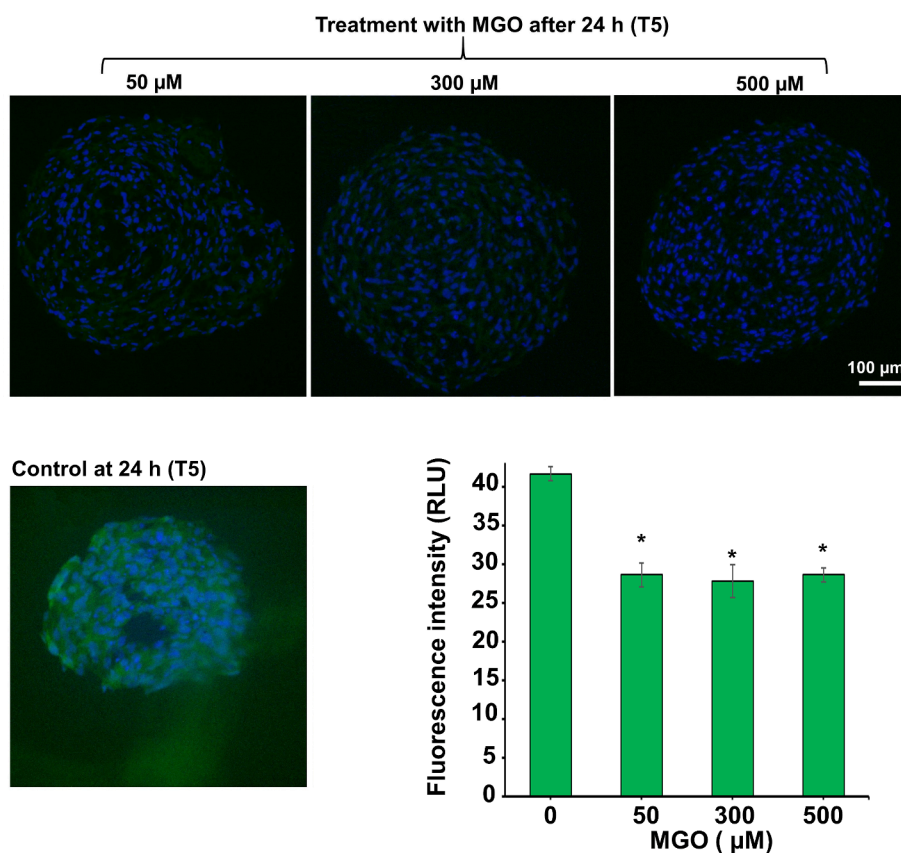


Fig. 9. Immunofluorescence images using Glo 1 antibody. Representative fluorescence merged microphotographs of 3D-hNLC spheroid sections of Glo1-positive after 24 h exposure to MGO (50, 300 and 500 μM). Nuclei were stained with Hoechst 33258. Fluorescence microscope images were taken using magnification X20. Bar chart represents the quantitative analysis of fluorescence intensity. Data are expressed as mean ± S.D.. *p < 0.05, different from control, statistical analysis by One-way ANOVA followed by Tukey's post hoc test.

at 100 μM after 24 h (Fig. 5). A significantly decrease of E-Cad expression was also observed from 100 μM MGO after 24 h persisting up to 48 h (Fig. 6).

The neuronal markers, MAP-2 and NSE, were reduced after 24 h

exposure from 50 μM MGO, and these effects occurred even at lower concentrations (10 μM) after 48 h (Fig. 7), while TuJ1 was not affected by any concentration (even at the higher ones; Fig. 8).

A concentration- and time-dependent decrease of Glo1 enzyme in

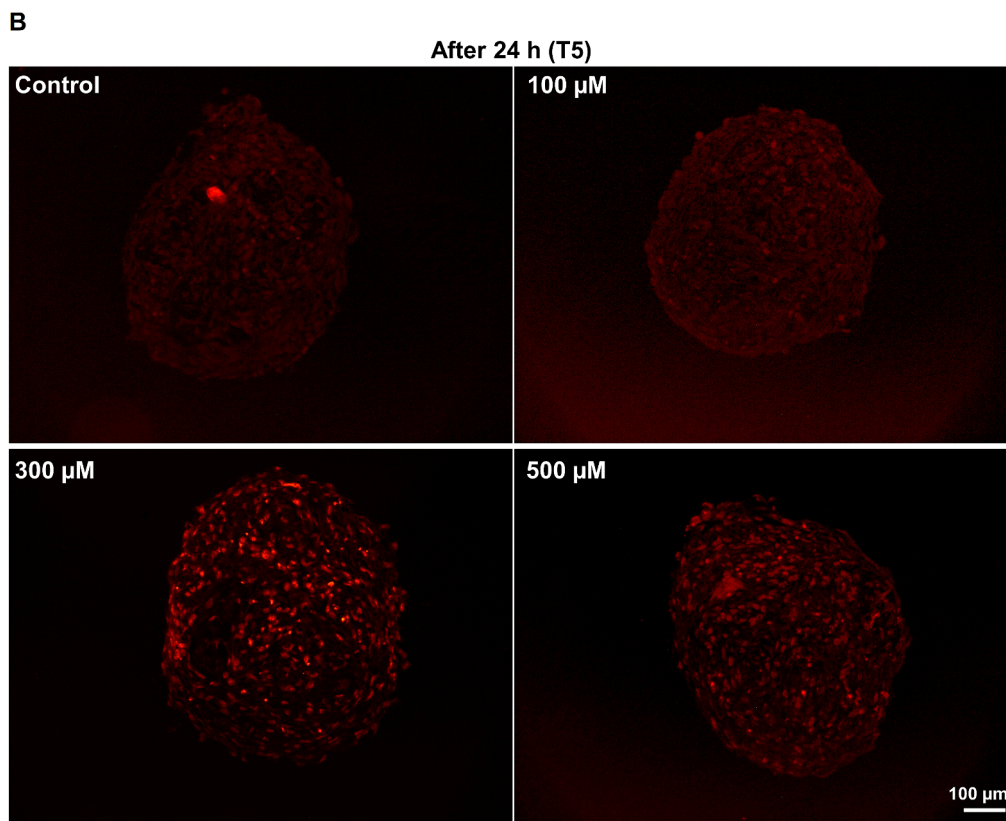
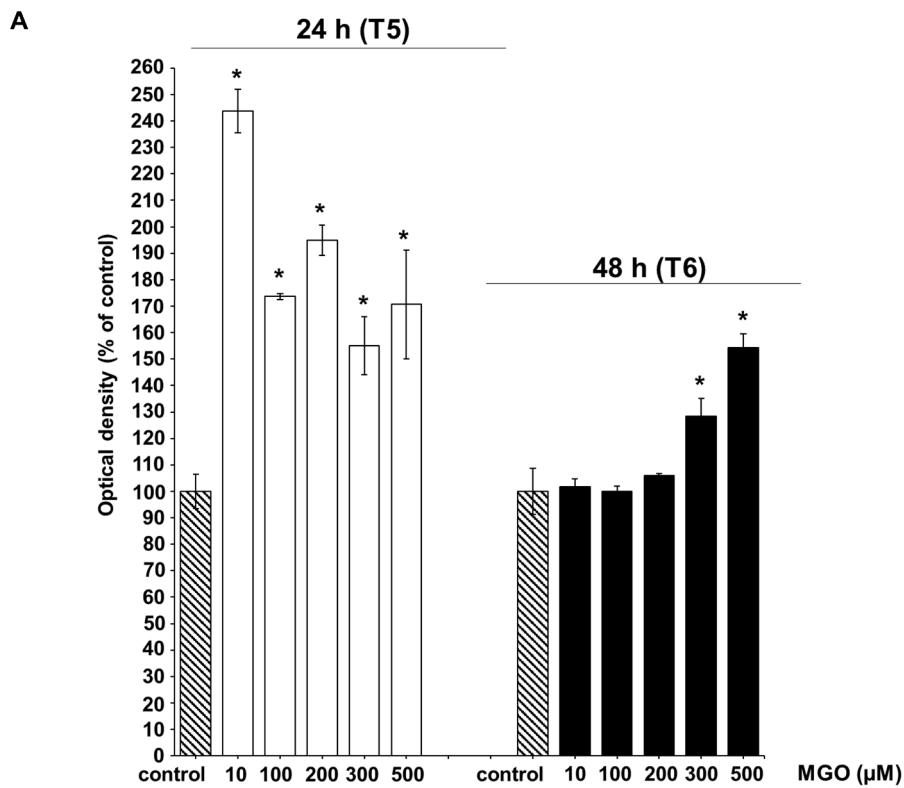


Fig. 10. NF-κB evaluation. A) phospho-NF-κB p65 evaluation in hNLCs spheroids exposed to increasing concentration of MGO for 24 and 48 h evaluated by ELISA assay. The data are expressed as mean ± S.D.. *p < 0.05, different from control, statistical analysis by One-way ANOVA followed by Tukey's post hoc test. B) Immunofluorescence of NF-κB by immunohistochemistry. Representative images of NF-κB-positive 3D-hNLCs after 24 h exposure to higher concentrations of MGO (300 and 500 μM). Fluorescence microscope images were taken using magnification X20.

treated-neurospheroids was induced by MGO starting from 50 μM after 24 h (Fig. 9).

NF- κB system was stimulated by MGO treatment as evidenced by both the increase of NF- κB p65 in cell lysates after 10 μM , and by the nuclear translocation of NF- κB p50 from cytoplasm after ≥ 300 μM in spheroid sections (Fig. 10).

Recent studies confirmed collagen as a main target for MGO modifications *in vivo* within the ECM in that MGO-collagen disrupted cell redox homeostasis, by directly generating hydrogen peroxide and oxygen derived free radicals, and induced endoplasmic reticulum stress and apoptosis (Nowotny et al., 2018). Also, collagen fibrils, which constitute a fundamental component of tissue at the nanoscale, are found to be highly susceptible to the accumulation of AGEs (Gautieri et al., 2017; Andriotis et al., 2019; Kamml et al., 2023). Although the specific mechanisms caused by these changes within the fibril structure remain poorly understood, it has been underlined that AGE functions, by both cross-linking or non-cross-linking, may affect the collagen properties in different ways: the non-cross-linking AGEs may cause changes in the tissue metabolism and protein function, whereas the cross-linking AGEs affect the mechanical behaviour of the collagen fibrils thus leading to changes at the tissue level (Kamml et al., 2023). For example, collagen glycation is frequently observed in neuroinflammatory and neurodegenerative disorders, such as Parkinson's and Alzheimer's diseases, osteoarthritis, diabetic neuropathy, amyloid polyneuropathy, and the aging process (Hudson and Lippman, 2018; Dandia et al., 2019; Bufalo et al., 2022). AGEs can activate specific cell surface receptors that transduce signals through downstream proteins, leading to the inflammatory process. Collagen glycation modifies the ECM structure and properties, resulting in pore size increase and matrix remodelling. This process may affect the optimal biochemical functions and cell-matrix component interactions, potentially disrupting cellular homeostasis (Dzobo and Dandara, 2023). Mechanical perturbations of the ECM may change cell behaviour, especially migration and invasion. Low presence of collagens may lead to the formation of spheroids that lacked cohesion, with the cells spreading towards the outer region of the spheroid.

Moreover, in MGO-treated neurospheroids, the decrease expression of E-Cad, one of the most important molecules in cell-cell adhesion and important key factor involves in the ability of cells to form compact spheroids (Casey et al., 2001; Enmon et al., 2002; Lin et al., 2006; Ivascu and Kubbies, 2007; Saias et al., 2015; Ivanov and Grabowska, 2017; Smyrek et al., 2019; Perez et al., 2023), is consistent with the evidences that AGE stimulation results in cleavage of cadherins from the cell surface. Downregulated expression of E-cadherin destroys the intracellular junction and thus cells acquire the ability to migrate and facilitates invasion. Expression decrease of E-Cad was observed in human colon cancer cells treated with various concentrations of AGEs (Liang, 2020).

Furthermore, linkage of the cadherin-catenin complex to the actin cytoskeleton, may control cytoskeleton function and thus junctional integrity (Sluysmans et al., 2017; Radeva and Waschke, 2018; Xu et al., 2018). The interaction between junctions and the cytoskeleton is crucial for tissue development and physiology, and is involved in the molecular mechanisms governing cell shape, motility, growth and signalling. Studies have demonstrated that AGEs can significantly increase endothelial monolayer permeability via disorganized endothelial F-actin cytoskeleton and VE-cadherin distribution (Guo et al., 2009; Xu et al., 2018). In neurons, AGE modifications have been shown to reorganize the cytoskeleton filaments (Bufalo et al., 2022). These effects are in line with our findings related to some specific neuronal markers, i.e. MAP-2 and NSE, belonging to those representing major components of cross-bridges between microtubules (MT) and neurofilaments in the cytoskeleton of neurons. In accordance with the traits of our results, a decreased number of MAP-2-positive neurons was also determined after addition of 100 μM MGO to primary culture of rat hippocampal neurons, wherein also their dendrites showed markedly retractile and tortuous appearances (Chen et al., 2010; Radu et al., 2012), and cellular neuronal level reduction of NSE occurred in 24 h-treated neuroblastoma cells (SK-

N-SH) with high concentrations of MGO (500 μM) (Haddad et al., 2019). The latter study suggested that the decreasing expression of NSE, along with other specific neuroprotectors and neurotrophic factors decreases (i.e., PRGN, MMP-9 and APP), caused by exposure to AGEs precursors, including MGO, might be capable to reduce the neurotrophic properties, neuritic growth, synaptogenesis, anti-inflammatory activity, and ability of neurons to degrade amyloid Beta, as well as modify the lysosome regulatory properties of neuronal cells.

MAP-2 is the predominant cytoskeletal regulator within neuronal dendrites, abundant and specific enough to serve as a robust somatodendritic marker (DeGiosio et al., 2022). MAP-2 is involved in the processes initiating and extending neurite-like outgrowths. The significant down-regulation of the cellular MAP-2 caused by MGO without altering the level of tubulin may indicate that MGO induces a rapid disorganization of cellular microtubule network before significantly reducing tubulin levels.

With respect to the MGO-induced Glo1 reduction, it is well known that, as the result of MGO formation/detoxification balance alteration, a dicarbonyl stress is fostered by a reduction in the expression or activity of Glo1 (Schalkwijk and Stehouwer, 2020). Dicarbonyls themselves may bind to reactive cysteine residues in the regulatory inhibitory protein of Nrf2, kelch-like ECH-associated protein 1 (Keap1), by disrupting the nuclear translocation of Nrf2, necessary to the transcriptional activation of Glo1 (Xue et al., 2015). This is also negatively regulated by HIF1- α (hypoxia-inducible factor 1- α) in hypoxia (Zhang et al., 2012), which is an important driver of dicarbonyl stress by both increasing MGO formation through anaerobic glycolysis and inhibiting Glo1 expression.

MGO has been shown to trigger NF- κB nuclear translocation in neuroblastoma cells (Wang et al., 2014) and both HIF1- α and NF- κB are known to downregulate Glo1 expression. The activation of NF- κB system in inflammation and downstream of the AGE/receptor of AGE (RAGE) pathway inhibits Nrf2, therefore downregulating Glo1 expression (Nigro et al., 2019; Gao et al., 2022).

Stimulation of the NF- κB system by MGO has been observed in the treated neurospheroids and once activated, NF- κB induces the transcription of several genes involved in different cellular processes. The disruption of this signal nexus may further contribute to the detected Glo1 decreases.

The Nrf2 and NF- κB pathways co-regulate cellular responses to oxidative stress and inflammation (Gao et al., 2022), and a large number of studies, investigating therapeutic drug-induced toxicity, indicate that in brain, inflammation and oxidative damage, may be prevented by up-regulating the gene expression level of the Nrf2/HO-1 pathway and by avoiding the induction of NF- κB activation (Jangra et al., 2016; Arafa and Atteia, 2020). Several reports have underlined the importance of the crosstalk of Nrf2 and NF- κB signal pathways in neurotoxicity/neuroprotection (Zhao et al., 2017) as well as the involvement of Nrf2 and NF- κB interplay in neurodegenerative disorders, in which the increase of NF- κB aggravates neuroinflammation while the increase of Nrf2 affords neuroprotection (Sivandzade et al., 2019). Therefore, regulation and dysregulation of NF- κB play a key role in diseases control (Shih et al., 2015). Normally, NF- κB is finely self-regulated for maintaining its basal activity avoiding an excessive transactivation and deleterious cellular responses (Giridharan and Srinivasan, 2018). The nucleo-cytoplasmic shuttling of p65 and its activation is critical for transcriptional regulation of target genes, including its own inhibitor I- $\kappa\text{B}\alpha$. The postinduction repression of NF- κB p65 by newly synthesized I- $\kappa\text{B}\alpha$ can be considered upstream events that assist in maintaining the homeostasis between the cytoplasmic and nuclear p65. Several strategies are being investigated to block p65 at each level along the signalling pathway with the final goal of a therapeutic application for improved clinical efficacy (Shih et al., 2015; Giridharan and Srinivasan, 2018).

Decreased expression of Glo1 occurs in the context of hyperglycaemia, inflammation, hypoxia, and oxidative stress (Schalkwijk and Stehouwer, 2020). Therefore, together with the increased MGO formation, Glo1 downregulation, by the mentioned above factors, provides the

conditions for dicarbonyl stress in several diseases such as diabetes and diabetic complications, atherosclerosis, hypertension, cancer, and disorders of the CNS (Masania et al., 2016; Schalkwijk and Stehouwer, 2020). In relation to CNS, it has been demonstrated that MGO is involved in the increased levels of AGEs observed in AD (Krautwald and Münch, 2010) and several MGO-derived AGEs have been identified in intracellular protein deposits in neurofibrillary tangles (Jono et al., 2002) and cerebrospinal fluid (Ahmed et al., 2005; see review of Angeloni et al., 2014; Nigro et al., 2017). Increased levels of AGEs are also observed in the brains of patients suffering from synucleinopathy including PD (Dalfó et al., 2005). Experimental studies evaluating the effects of MGO in different models of Parkinson's disease, corroborated that glycation promotes α -synuclein-mediated toxicity and aggregation in cell models of PD (i.e. yeast, H4 neuroglioma, LUHMES, PD iPSCs), and promotes neuronal loss in mice and decreases motor performance in *Drosophila* (Vicente Miranda et al., 2017).

Dicarbonyl stress produces increased *in situ* rates of glycation by dicarbonyls of proteins, DNA and basic phospholipids, as reactive dicarbonyls are unquestionably relevant players in PD and AD pathogenesis, and also contributes to aging through the age-related decline in Glo1 even in human brain (Nigro et al., 2017). MGO-derived AGEs were reported to be increased in aging tissues and, considering that on a molecular level, various hallmarks have been reported (López-Otín et al., 2013) to explain the aging process, many of these aging-related molecular events could be fostered by dicarbonyl accumulation, which thus represents a determinant of the aging phenotype.

Clearly when the accumulation of MGO exceeds the physiological cellular levels, dicarbonyl stress occurs as a consequence of the imbalance between the generation/exposure and MGO metabolism (Nigro et al., 2017; Scirè et al., 2022). Noteworthy, in the present study, the lowest effective MGO concentration, namely, 5–10 μ M, is, on the other hand, more likely similar to that measured in plasma of patients with aging-related diseases, such as diabetes and AD disease, and thus clearly higher than that is expected under physiological conditions (Li et al., 2013). MGO plasma concentrations in healthy individuals are around 50–500 nM, intracellularly around 1–4 μ M, and in brain 0.3–1.5 μ M (Rabbani and Thornalley, 2014; Scheijen and Schalkwijk, 2014; Kold-Christensen and Johannsen, 2020; Rabbani et al., 2020; Lai et al., 2022).

The cytotoxic effects observed by using this human 3D cell-based model of neurons occurred from 5–10 μ M MG confirming previous findings obtained on 2D mono-layer neuron-like cells, thus strengthening once again that MGO-induced effects at concentrations much lower than those inducing toxicity in others *in vitro* models such as human neuroblastoma cell lines, animal primary cells, and human iPSCs (Coccini et al., 2023). In addition, MGO markedly affected, already after 24 h treatment, the neuronal markers MAP-2 and NSE causing their loss from 10–50 μ M, the Glo1 enzyme that significantly decreased from 50 μ M, and increased the NF- κ B expression from 10 μ M.

Most noteworthy, by using the 3D cell culture model of neurons, been capable of simulating key features of an *in vivo* tissue environment, was possible to evidence cytochemical alterations (50–100 μ M MGO treatments), occurring at morphological level and spheroid compactness, and modifications of cell–cell and cell-ECM interactions as revealed by decreases of cell-matrix components such as collagen and E-Cad.

Collectively the results provided advances and innovative insights in MGO neurotoxicity by using the 3D neurospheroid system in relation to its structural characteristics like morphology, proliferation, and cell communications. This approach enables to expand the preclinical experimental toolbox making it more reliable and predictive within the neurotoxicity evaluation.

The neurospheroid system, can be applied as a valuable human cell-based relevant assay within an *in vitro* test battery designed for neurotoxicological predictive studies and related AOP (adverse outcome pathway). The mechanistically based approach, applied by employing 3D spheroids, emphasizes on measurable endpoints, Molecular Initial

Events (MIE) (i.e. cell-growth, viability, neuronal markers, Glo 1, cell–cell/ECM components, NF- κ B) that have been altered by low MGO levels and known to be involved in the pathogenesis of neurodegeneration and aging. This implemented human stem-cell-derived 3D neurospheroid platform enables some weight-of-evidence that address toxicological pathways involved in MGO–induce neuronal effects.

5. Conclusion

The findings of the present study, first of all, corroborate the importance of developing the human-based 3D spheroid model, namely stem-cell-derived neuronal spheroids, that, recapitulating *in vivo* tissue-like architecture, consider different features including the ECM components, *in vivo* multi-cellular microenvironments and reconstruction biological signal pathways of cell–cell and cell-ECM interactions, which encourage proliferation and viability of cells.

Secondly, the data obtained with the human 3D neuronal spheroids indicate that MGO, the most potent glycating agent in humans, in the low-ten micromolar range, nonetheless comparable to human samples levels measured in MGO-associated diseases, is effective in modifying neuronal key signalling molecules/endpoints relevant as molecular hallmarks (Filadi and Pizzo, 2022; Wilson et al., 2023) of biochemical pathways involved in facilitating the pathological cascades underlying neurodegenerative diseases and aging. Given the involvement of the highly reactive AGE precursor MGO and MGO-derived AGEs in several pathologies including neurodegenerative disorders (Li et al., 2012; Angeloni et al., 2014), it arises necessarily the need to further carry out advanced studies of the effects, of such heterogeneous, complex group of compounds, on neuronal function, by applying valuable tools, like human neuronal cells, preferably 3D model, as well as new advanced *in vitro* models.

The complex spheroid system is also ideal for detection of adverse effects considering an *in vitro* long-term and repeated exposure, that mimic chronic conditions. Moreover, applying hetero-type 3D multi-cellular spheroids, by the assembly/co-culture of neurons and astrocytes, reproducing features that are even more similar to brain tissue, it is possible to evaluate the impact of the astrocyte presence in counteracting the MGO-induced neuronal toxic effects. Innovative *in vitro* cellular models should also address the potential role of various cell types linked to the neuronal lineage (e.g. astrocytes, oligodendrocytes), vascular lineage (e.g. endothelial cells, pericytes), or myeloid lineage (i.e. microglia) which have important implications in MGO metabolism/toxicity, transport across the blood brain barrier (e.g. MGO exogenous), or internal to the neural compartment (endogenous).

Declaration of competing interest

The authors declare that they have no known competing financial interests or personal relationships that could have appeared to influence the work reported in this paper.

Data availability

Data will be made available on request.

Acknowledgment

This work was supported in part by the Ricerca Corrente funding scheme of the Ministry of Health, Italy.

References

- Ahmed, N., Ahmed, U., Thornalley, P.J., Hager, K., Fleischer, G., Münch, G., 2005. Protein glycation, oxidation and nitration adduct residues and free adducts of cerebrospinal fluid in Alzheimer's disease and link to cognitive impairment. *J. Neurochem.* 92 (2), 255–263. <https://doi.org/10.1111/j.1471-4159.2004.02864.x>.

- Allaman, I., Bélanger, M., Magistretti, P.J., 2015. Methylglyoxal, the dark side of glycolysis. *Front. Neurosci.* 9, 23. <https://doi.org/10.3389/fnins.2015.00023>.
- Andriotis, O.G., Elsayad, K., Smart, D.E., Nalbach, M., Davies, D.E., Thurner, P.J., 2019. Hydration and nanomechanical changes in collagen fibrils bearing advanced glycation end-products. *Biomed. Opt. Express.* 10 (4), 1841–1855. <https://doi.org/10.1364/BOE.10.001841>.
- Angeloni, C., Zamboni, L., Hrelia, S., 2014. Role of methylglyoxal in Alzheimer's disease. *Biomed. Res. Int.* 2014, 238485 <https://doi.org/10.1155/2014/238485>.
- Arafa, M.H., Attea, H.H., 2020. Protective role of epigallocatechin gallate in a rat model of cisplatin-induced cerebral inflammation and oxidative damage: impact of modulating NF- κ B and Nrf2. *Neurotox. Res.* 37 (2), 380–396. <https://doi.org/10.1007/s12640-019-00095-x>.
- Bufalo, M.C., de Almeida, M.E.S., Jensen, J.R., DeOcesano-Pereira, C., Lichtenstein, F., Picolo, G., Chudzinski-Tavassi, A.M., Coccuzzo Sampaio, S., Cury, Y., Olzon Zambelli, V., 2022. Human sensory neuron-like cells and glycated collagen matrix as a model for the screening of analgesic compounds. *Cells* 11 (2), 247. <https://doi.org/10.3390/cells11020247>.
- Casey, R.C., Burleson, K.M., Skubitz, K.M., Pambuccian, S.E., Oegema, T.R., Ruff, L.E., Skubitz, A.P., 2001. Beta 1-integrins regulate the formation and adhesion of ovarian carcinoma multicellular spheroids. *Am. J. Pathol.* 159, 2071–2080. [https://doi.org/10.1016/S0002-9440\(10\)63058-1](https://doi.org/10.1016/S0002-9440(10)63058-1).
- Chen, Y.J., Huang, X.B., Li, Z.X., Yin, L.L., Chen, W.Q., Li, L., 2010. Tenuigenin protects cultured hippocampal neurons against methylglyoxal-induced neurotoxicity. *Eur. J. Pharmacol.* 645 (1–3), 1–8. <https://doi.org/10.1016/j.ejphar.2010.06.034>.
- Chen, Y., Yu, Q., Xu, C.B., 2017. A convenient method for quantifying collagen fibers in atherosclerotic lesions by ImageJ software. *Int. J. Clin. Exp. Med.* 10 (10), 14904–14910. www.ijcem.com/ISSN:1940-5901/IJCEM0059973.
- Choudhary, P., Gupta, A., Gupta, S.K., Dwivedi, S., Singh, S., 2024. Comparative evaluation of divergent concoction of NGF, BDNF, EGF, and FGF growth factor's role in enhancing neuronal differentiation of adipose-derived mesenchymal stem cells. *Int. J. Biol. Macromol.* 260 (Pt 2), 129561 <https://doi.org/10.1016/j.ijbiomac.2024.129561>.
- Coccini, T., De Simone, U., Roccio, M., Croce, S., Lenta, E., Zecca, M., Spinillo, A., Avanzini, M.A., 2019. In vitro toxicity screening of magnetite nanoparticles by applying mesenchymal stem cells derived from human umbilical cord lining. *J. Appl. Toxicol.* 39 (9), 1320–1336. <https://doi.org/10.1002/jat.3819>.
- Coccini, T., Spinillo, A., Roccio, M., Lenta, E., Valsecchi, C., De Simone, U., 2022. Human umbilical cord mesenchymal stem cell-based in vitro model for neurotoxicity testing. *Curr. Prot.* 2 (4), e423.
- Coccini, T., Schicchi, A., Locatelli, C.A., Caloni, F., Negri, S., Grignani, E., De Simone, U., 2023. Methylglyoxal-induced neurotoxic effects in primary neuronal-like cells transdifferentiated from human mesenchymal stem cells: impact of low concentrations. *J. Appl. Toxicol.* 1–21 <https://doi.org/10.1002/jat.4515>.
- Conti Mazza, M., Shuck, S.C., Lin, J., Moxley, M.A., Termini, J., Cookson, M.R., Wilson, M.A., 2022. DJ-1 is not a deglycase and makes a modest contribution to cellular defense against methylglyoxal damage in neurons. *J. Neurochem.* 162 (3), 245–261. <https://doi.org/10.1111/jnc.15656>.
- Currais, M., Maher, P., 2013. Functional consequences of age-dependent changes in glutathione status in the brain. *Antioxid. Redox. Signal.* 19 (8), 813–822. <https://doi.org/10.1089/ars.2012.4996>.
- Dalfo, E., Portero-Otín, M., Ayala, V., Martínez, A., Pamplona, R., Ferrer, I., 2005. Evidence of oxidative stress in the neocortex in incidental Lewy body disease. *J. Neuropathol. Exp. Neurol.* 64 (9), 816–830. <https://doi.org/10.1097/01.jen.0000179050.54522.5a>.
- Dandia, H., Makkad, K., Tayalia, P., 2019. Glycated collagen-A 3D matrix system to study pathological cell behavior. *Biomater. Sci.* 7 (8), 3480–3488. <https://doi.org/10.1039/c9bm00184k>.
- De Simone, U., Croce, A.C., Pignatti, P., Buscaglia, E., Caloni, F., Coccini, T., 2022. Three-dimensional spheroid cell culture of human MSC-derived neuron-like cells: new in vitro model to assess magnetite nanoparticle-induced neurotoxicity effects. *J. Appl. Toxicol.* 42 (7), 1230–1252. <https://doi.org/10.1002/jat.4292>.
- DeGosio, R.A., Grubisha, M.J., MacDonald, M.L., McKinney, B.C., Camacho, C.J., Sweet, R.A., 2022. More than a marker: potential pathogenic functions of MAP2. *Front. Mol. Neurosci.* 15, 974890 <https://doi.org/10.3389/fnmol.2022.974890>.
- Derk, J., MacLean, M., Juranek, J., Schmidt, A.M., 2018. The receptor for advanced glycation endproducts (RAGE) and mediation of inflammatory neurodegeneration. *J. Alzheimers Dis. Parkinsonism.* 8 (1), 421. <https://doi.org/10.4172/2161-0460.1000421>.
- Dzobo, K., Dandara, C., 2023. The Extracellular Matrix: its composition, function, remodelling, and role in tumorigenesis. *Biomimetics.* 8 (2), 146. <https://doi.org/10.3390/biomimetics8020146>.
- Enmon, R.M., O'Connor, K.C., Song, H., Lacks, D.J., Schwartz, D.K., 2002. Aggregation kinetics of well and poorly differentiated human prostate cancer cells. *Biotechnol. Bioeng.* 80, 580–588. <https://doi.org/10.1002/bit.10394>.
- Fessel, G., Li, Y., Diederich, V., Guizar-Sicairos, M., Schneider, P., Sell, D.R., Monnier, V.M., Snedeker, J.G., 2014. Advanced glycation end-products reduce collagen molecular sliding to affect collagen fibril damage mechanisms but not stiffness. *PLoS ONE* 9 (11), e110948.
- Filadi, R., Pizzo, P., 2022. Key signalling molecules in aging and neurodegeneration. *Cells* 11 (5), 834. <https://doi.org/10.3390/cells11050834>.
- Gao, W., Guo, L., Yang, Y., Wang, Y., Xia, S., Gong, H., Zhang, B.-K., Yan, M., 2022. Dissecting the crosstalk between Nrf2 and NF- κ B response pathways in drug-induced toxicity. *Front. Cell Dev. Biol.* 9, 809952 <https://doi.org/10.3389/fcell.2021.809952>.
- Gautieri, A., Passini, F.S., Silván, U., Guizar-Sicairos, M., Carimati, G., Volpi, P., Moretti, M., Schoenhuber, H., Redaelli, A., Berli, M., Snedeker, J.G., 2017. Advanced glycation end-products: mechanics of aged collagen from molecule to tissue. *Matrix Biol.* 59, 95–108. <https://doi.org/10.1016/j.matbio.2016.09.001>.
- Girdharan, S., Srinivasan, M., 2018. Mechanisms of NF- κ B p65 and strategies for therapeutic manipulation. *J. Inflamm. Res.* 11, 407–419. <https://doi.org/10.2147/JIR.S410188>.
- Guo, X., Wang, L., Chen, B., Li, Q., Wang, J., Zhao, M., Wu, W., Zhu, P., Huang, X., Huang, Q., 2009. ERM protein moesin is phosphorylated by advanced glycation end products and modulates endothelial permeability. *Am. J. Physiol. Heart Circ. Physiol.* 297(1), H238–H246. doi: 10.1152/ajpheart.00196.2009.
- Gupta, A., Singh, S., 2022. Potential role of growth factors controlled release in achieving enhanced neuronal trans-differentiation from mesenchymal stem cells for neural tissue repair and regeneration. *Mol. Neurobiol.* 59, 983–1001. <https://doi.org/10.1007/s12035-021-02646-w>.
- Haddad, M., Perrotte, M., Khedher, M.R.B., Demongin, C., Lepage, A., Fülöp, T., Ramassamy, C., 2019. Methylglyoxal and glyoxal as potential peripheral markers for MCI diagnosis and their effects on the expression of neurotrophic, inflammatory and neurodegenerative factors in neurons and in neuronal derived-extracellular vesicles. *Int. J. Mol. Sci.* 20 (19), 4906. <https://doi.org/10.3390/ijms20194906>.
- Hara, T., Toyoshima, M., Hisano, Y., Balan, S., Iwayama, Y., Aono, H., Futamura, Y., Osada, H., Owada, Y., Yoshikawa, T., 2021. Glyoxalase I disruption and external carbonyl stress impair mitochondrial function in human induced pluripotent stem cells and derived neurons. *Transl. Psychiatry* 11 (1), 275. <https://doi.org/10.1038/s41398-021-01392-w>.
- Hogberg, H.T., de Cássia da Silveira E Sá, R., Kleinsang, A., Bouhifd, M., Cemilgolu Ulker, O., Smirnova, L., Behl, M., Maertens, A., Zhao, L., Hartung, T., 2021. Organophosphorus flame retardants are developmental neurotoxicants in a rat primary brain sphere in vitro model. *Arch. Toxicol.* 95(1), 207–228. doi: 10.1007/s00204-020-02903-2.
- Hudson, B.L., Lippman, M.E., 2018. Targeting RAGE signaling in inflammatory disease. *Annu. Rev. Med.* 69, 349–364. <https://doi.org/10.1146/annurev-med-041316-085215>.
- Ivanov, D.P., Grabowska, A.M., 2017. Spheroid arrays for high throughput single cell analysis of spatial patterns and biomarker expression in 3D. *Sci. Rep.* 7, 41160.
- Ivascu, A., Kubbies, M., 2007. Diversity of cell-mediated adhesions in breast cancer spheroids. *Int. J. Oncol.* 31, 1403–1413. <https://doi.org/10.3892/ijo.31.6.1403>.
- Jangra, A., Kwatra, M., Singh, T., Pant, R., Kushwah, P., Ahmed, S., Dwivedi, D., Saroha, B., Lahkar, M., 2016. Edaravone alleviates cisplatin-induced neurobehavioral deficits via modulation of oxidative stress and inflammatory mediators in the rat hippocampus. *Eur. J. Pharmacol.* 791, 51–61. <https://doi.org/10.1016/j.ejphar.2016.08.003>.
- Jono, T., Kimura, T., Takamatsu, J., Nagai, R., Miyazaki, K., Yuzuriha, T., Kitamura, T., Horiuchi, S., 2002. Accumulation of imidazolone, pentosidine and N-(carboxymethyl)lysine in hippocampal CA4 pyramidal neurons of aged human brain. *Pathol. Inter.* 52 (9), 563–571. <https://doi.org/10.1046/j.1320-5463.2002.01390.x>.
- Jorfi, M., D'Avanzo, C., Kim, D.Y., Irimia, D., 2018. Three-dimensional models of the human brain development and diseases. *Adv. Healthc. Mater.* 7 (1), 1–36. <https://doi.org/10.1002/adhm.201700723>.
- Kaltschmidt, B., Helweg, L.P., Greiner, J.F.W., Kaltschmidt, C., 2022. NF- κ B in neurodegenerative diseases: Recent evidence from human genetics. *Front. Mol. Neurosci.* 15, 954541 <https://doi.org/10.3389/fnmol.2022.954541>.
- Kaltschmidt, B., Kaltschmidt, C., 2009. NF- κ B in the nervous system. *Cold Spring Harb. Perspect. Biol.* 1 (3), a001271 <https://doi.org/10.1101/cshperspect.a001271>.
- Kamml, J., Ke, C.Y., Acevedo, C., Kammer, D.S., 2023. The influence of AGEs and enzymatic cross-links on the mechanical properties of collagen fibrils. *J. Mech. Behav. Biomed. Mater.* 143, 105870 <https://doi.org/10.1016/j.jmbmm.2023.105870>.
- Kim, T.W., Che, J.H., Yun, J.W., 2019. Use of stem cells as alternative methods to animal experimentation in predictive toxicology. *Regul. Toxicol. Pharmacol.* 105, 15–29. <https://doi.org/10.1016/j.yrtph.2019.03.016>.
- Kitamura, K., Umehara, K., Ito, R., Yamaura, Y., Komori, T., Morio, H., Akita, H., Furihata, T., 2021. Development, characterization and potential applications of a multicellular spheroidal human blood-brain barrier model integrating three conditionally immortalized cell lines. *Biol. Pharm. Bull.* 44 (7), 984–991. <https://doi.org/10.1248/bpb.b21-00218>.
- Kold-Christensen, R., Johannsen, M., 2020. Methylglyoxal metabolism and aging-related disease: moving from correlation toward causation. *Trends Endocrinol. Metab.* 31 (2), 81–92. <https://doi.org/10.1016/j.tem.2019.10.003>.
- Kong, X., Ma, M., Huang, K., Qin, L., Zhang, H., Yang, Z., Li, X., Su, Q., 2014. Increased plasma levels of the methylglyoxal in patients with newly diagnosed type 2 diabetes. *J. Diabetes* 6 (6), 535–540. <https://doi.org/10.1111/1753-0407.12160>.
- Kosheleva, N.V., Efreimov, Y.M., Shavkuta, B.S., Zurina, I.M., Zhang, D., Minaev, N.V., Gorkun, A.A., Wei, S., Shpichka, A.I., Saburina, I.N., Timashev, P.S., 2020. Cell spheroid fusion: beyond liquid drops model. *Sci. Rep.* 10 (1), 12614. <https://doi.org/10.1038/s41598-020-69540-8>.
- Krautwald, M., Münch, G., 2010. Advanced glycation end products as biomarkers and gerontotoxins—a basis to explore methylglyoxal-lowering agents for Alzheimer's disease? *Exp. Gerontol.* 45 (10), 744–751. <https://doi.org/10.1016/j.exger.2010.03.001>.
- Kuhla, B., Luth, H.J., Haferburg, D., Boeck, K., Arendt, T., Munch, G., 2005. Methylglyoxal, glyoxal, and their detoxification in Alzheimer's disease. *Ann. N.Y. Acad. Sci.* 1043, 211–216. <https://doi.org/10.1196/annals.1333.026>.
- Lai, S.W.T., Lopez Gonzalez, E.D.J., Zoukari, T., Ki, P., Shuck, S.C., 2022. Methylglyoxal and its adducts: induction, repair, and association with disease. *Chem. Res. Toxicol.* 35 (10), 1720–1746. <https://doi.org/10.1021/acs.chemrestox.2c00160>.

- Levy, Y.S., Merims, D., Panet, H., Barhum, Y., Melamed, E., Offen, D., 2003. Induction of neuron-specific enolase promoter and neuronal markers in differentiated mouse bone marrow stromal cells. *J. Mol. Neurosci.* 21 (2), 121–132. <https://doi.org/10.1385/JMN:21:2:121>.
- Li, X.H., Du, L.L., Cheng, X.S., Jiang, X., Zhang, Y., Lv, B.L., Liu, R., Wang, J.Z., Zhou, X.W., 2013. Glycation exacerbates the neuronal toxicity of β -amyloid. *Cell Death Dis.* 4 (6), e673.
- Li, J., Liu, D., Sun, L., Lu, Y., Zhang, Z., 2012. Advanced glycation end products and neurodegenerative diseases: mechanisms and perspective. *J. Neurol. Sci.* 317 (1–2), 1–5. <https://doi.org/10.1016/j.jns.2012.02.018>.
- Liang, H., 2020. Advanced glycation end products induce proliferation, invasion and epithelial-mesenchymal transition of human SW480 colon cancer cells through the PI3K/AKT signaling pathway. *Oncol. Lett.* 19 (4), 3215–3222. <https://doi.org/10.3892/ol.2020.11413>.
- Lin, C.C., Chan, C.M., Huang, Y.P., Hsu, S.H., Huang, C.L., Tsai, S.J., 2016. Methylglyoxal activates NF- κ B nuclear translocation and induces COX-2 expression via a p38-dependent pathway in synovial cells. *Life Sci.* 149, 25–33. <https://doi.org/10.1016/j.lfs.2016.02.060>.
- Lin, R.Z., Chou, L.F., Chien, C.C.M., Chang, H.Y., 2006. Dynamic analysis of hepatoma spheroid formation: roles of E-cadherin and β 1-integrin. *Cell Tissue Res.* 324, 411–422. <https://doi.org/10.1007/s00441-005-0148-2>.
- López-Otín, C., Blasco, M.A., Partridge, L., Serrano, M., Kroemer, G., 2013. The hallmarks of aging. *Cell* 153 (6), 1194–1217. <https://doi.org/10.1016/j.cell.2013.05.039>.
- Masania, J., Malczewska-Malec, M., Razny, U., Goralska, J., Zdzienicka, A., Kiec-Wilk, B., Gruca, A., Stancel-Mozwillo, J., Dembinska-Kiec, A., Rabbani, N., Thornalley, P.J., 2016. Dicarbonyl stress in clinical obesity. *Glycoconj. J.* 33 (4), 581–589. <https://doi.org/10.1007/s10719-016-9692-0>.
- McLellan, A.C., Thornalley, P.J., Benn, J., Sonksen, P.H., 1994. Glyoxalase system in clinical diabetes mellitus and correlation with diabetic complications. *Clin. Sci. (Lond.)* 87 (1), 21–29. <https://doi.org/10.1042/cs0870021>.
- Miyazawa, N., Abe, M., Souma, T., Tanemoto, M., Abe, T., Nakayama, M., Ito, S., 2010. Methylglyoxal augments intracellular oxidative stress in human aortic endothelial cells. *Free Radic. Res.* 44 (1), 101–107. <https://doi.org/10.3109/10715760903321788>.
- Nass, N., Bartling, B., Navarrete Santos, A., Scheubel, R.J., Börgermann, J., Silber, R.E., Simm, A., 2007. Advanced glycation end products, diabetes and ageing. *Z. Gerontol. Geriatr.* 40 (5), 349–356. <https://doi.org/10.1007/s00391-007-0484-9>.
- Nigro, C., Leone, A., Raciti, G.A., Longo, M., Mirra, P., Formisano, P., Beguinot, F., Miele, C., 2017. Methylglyoxal-glyoxalase 1 balance: the root of vascular damage. *Int. J. Molec. Sci.* 18 (1), 188. <https://doi.org/10.3390/ijms18010188>.
- Nigro, C., Leone, A., Fiory, F., Prevenzano, I., Nicolò, A., Mirra, P., Beguinot, F., Miele, C., 2019. Dicarbonyl stress at the crossroads of healthy and unhealthy aging. *Cells* 8 (7), 749. <https://doi.org/10.3390/cells8070749>.
- Nowotny, K., Castro, J.P., Hugo, M., Braune, S., Weber, D., Pignitter, M., Somoza, V., Bornhorst, J., Schwerdtle, T., Grune, T., 2018. Oxidants produced by methylglyoxal-modified collagen trigger ER stress and apoptosis in skin fibroblasts. *Free Radic. Biol. Med.* 120, 102–113. <https://doi.org/10.1016/j.freeradbiomed.2018.03.022>.
- Perez, J.E., Jan, A., Villard, C., Wilhelm, C., 2023. Surface tension and neuronal sorting in magnetically engineered brain-like tissue. *Adv. Sci. (weinh)* 10 (27), e2302411.
- Piazza, M., Hanssen, N.M.J., Persson, F., Scheijen, J.L., van de Waarenburg, M.P.H., van Greevenbroek, M.M.J., Rossing, P., Hovind, P., Stehouwer, C.D.A., Parving, H.H., Schalkwijk, C.G., 2021. Irbesartan treatment does not influence plasma levels of the dicarbonyls methylglyoxal, glyoxal and 3-deoxyglucosone in participants with type 2 diabetes and microalbuminuria: an IRMA2 substudy. *Diabet. Med.* 38 (9), e14405.
- Rabbani, N., Xue, M., Thornalley, P.J., 2020. Dicarbonyl stress and the glyoxalase system. Chapter 36 – Oxidative Stress – Ed. Helmut Sies, Elsevier Academic Press, 2020, 759–777. doi: 10.1016/B978-0-12-818606-0.00036-5.
- Rabbani, N., Thornalley, P.J., 2008. Dicarbonyls linked to damage in the powerhouse: glycation of mitochondrial proteins and oxidative stress. *Biochem. Soc. Trans.* 36, 1045–1050. <https://doi.org/10.1042/BST0361045>.
- Rabbani, N., Thornalley, P.J., 2014. Dicarbonyl proteome and genome damage in metabolic and vascular disease. *Biochem. Soc. Trans.* 42 (2), 425–432. <https://doi.org/10.1042/BST20140018>.
- Rabbani, N., Xue, M., Thornalley, P.J., 2016. Methylglyoxal-induced dicarbonyl stress in aging and disease: First steps towards glyoxalase 1-based treatments. *Clin. Sci.* 130 (19), 1677–1696. <https://doi.org/10.1042/CS20160025>.
- Radeva, M.Y., Waschke, J., 2018. Mind the gap: mechanisms regulating the endothelial barrier. *Acta Physiol. (oxf)* 222 (1). <https://doi.org/10.1111/apha.12860>.
- Radu, B.M., Dumitrescu, D.I., Mustaciosu, C.C., Radu, M., 2012. Dual effect of methylglyoxal on the intracellular Ca²⁺ signalling and neurite outgrowth in mouse sensory neurons. *Cell. Mol. Neurobiol.* 32 (6), 1047–1057. <https://doi.org/10.1007/s10571-012-9823-5>.
- Roper, S.J., Linke, F., Scotting, P.J., Coyle, B., 2021. 3D spheroid models of paediatric SHH medulloblastoma mimic tumour biology, drug response and metastatic dissemination. *Sci. Rep.* 11 (1), 4259. <https://doi.org/10.1038/s41598-021-83809-6>.
- Rungratanawanich, W., Qu, Y., Wang, X., Essa, M.M., Song, B.J., 2021. Advanced glycation end products (AGEs) and other adducts in aging-related diseases and alcohol-mediated tissue injury. *Exp. Mol. Med.* 53 (2), 168–188. <https://doi.org/10.1038/s12276-021-00561-7>.
- Saias, L.A., Gomes, M., Ducommun, C.B., Lobjois, V., 2015. Cell-cell adhesion and cytoskeleton tension oppose each other in regulating tumor cell aggregation. *Cancer Res.* 75, 2426–2433. <https://doi.org/10.1158/0008-5472.CAN-14-3534>.
- Sanchez-Ramos, J., Song, S., Cardozo-Pelaez, F., Hazzi, C., Stedeford, T., Willing, A., Freeman, T.B., Saporta, S., Janssen, W., Patel, N., Cooper, D.R., Sanberg, P.R., 2000. Adult bone marrow stromal cells differentiate into neural cells in vitro. *Exp. Neurol.* 164 (2), 247–256. <https://doi.org/10.1006/exnr.2000.7389>.
- Schalkwijk, C.G., Stehouwer, C.D.A., 2020. Methylglyoxal, a highly reactive dicarbonyl compound, in diabetes, its vascular complications, and other age-related diseases. *Physiol. Rev.* 100 (1), 407–461. <https://doi.org/10.1152/physrev.00001.2019>.
- Scheijen, J.L., Schalkwijk, C.G., 2014. Quantification of glyoxal, methylglyoxal and 3-deoxyglucosone in blood and plasma by ultra performance liquid chromatography tandem mass spectrometry: evaluation of blood specimen. *Clin. Chem. Lab. Med.* 52 (1), 85–91. <https://doi.org/10.1515/cclm-2012-0878>.
- Scirè, A., Cianfruglia, L., Minelli, C., Romaldi, B., Laudadio, E., Galeazzi, R., Antognelli, C., Armeni, T., 2022. Glyoxalase 2: towards a broader view of the second player of the glyoxalase system. *Antioxidants (basel, Switzerland)* 11 (11), 2131. <https://doi.org/10.3390/antiox11112131>.
- Shih, R.H., Wang, C.Y., Yang, C.M., 2015. NF- κ B signaling pathways in neurological inflammation: a mini review. *Front. Mol. Neurosci.* 18, 8–77. <https://doi.org/10.3389/fnmol.2015.00077>.
- Shima, F., Makino, T., 2022. Construction of brain-like spheroids containing endothelial tubular networks by an adhesive culture system. *Biochem. Biophys. Res. Commun.* 623, 176–180. <https://doi.org/10.1016/j.bbrc.2022.07.063>.
- Singh, A.K., Kashyap, M.P., 2016. An overview on human umbilical cord blood stem cell-based alternative in vitro models for developmental neurotoxicity assessment. *Mol. Neurobiol.* 53 (5), 3216–3226. <https://doi.org/10.1007/s12035-015-9202-6>.
- Sivandzade, F., Prasad, S., Bhalerao, A., Cucullo, L., 2019. NRF2 and NF- κ B interplay in cerebrovascular and neurodegenerative disorders: molecular mechanisms and possible therapeutic approaches. *Redox Biol.* 21, 101059. <https://doi.org/10.1016/j.redox.2018.11.017>.
- Sluysmans, S., Vasileva, E., Spadaro, D., Shah, J., Rouaud, F., Citi, S., 2017. The role of apical cell-cell junctions and associated cytoskeleton in mechanotransduction. *Biol. Cell* 109, 139–161. <https://doi.org/10.1111/boc.201600075>.
- Smirnova, L., Hartung, T., 2024. The promise and potential of brain organoids. *Adv. Healthc. Mater.* 22, e2302745.
- Smyrek, I., Mathew, B., Fischer, S.C., Lissek, S.M., Becker, S., Stelzer, E.H.K., 2019. E-cadherin, actin, microtubules and FAK dominate different spheroid formation phases and important elements of tissue integrity. *Biol. Open* 8 (1), bio037051. <https://doi.org/10.1242/bio.037051>.
- Srikanth, V., Westcott, B., Forbes, J., Phan, T.G., Beare, R., Venn, A., Pearson, S., Greenaway, T., Parameswaran, V., Münch, G., 2013. Methylglyoxal, cognitive function and cerebral atrophy in older people. *J. Gerontol. A Biol. Sci. Med. Sci.* 68 (1), 68–73. <https://doi.org/10.1093/gerona/gls100>.
- Suh, K.S., Chon, S., Jung, W.W., Choi, E.M., 2022. Protective effects of sciadopitysin against methylglyoxal-induced degeneration in neuronal SK-N-MC cells. *J. Appl. Toxicol.* 42 (2), 274–284. <https://doi.org/10.1002/jat.4211>.
- Suma, R.N., Mohanan, P.V., 2015. Stem cells, a new generation model for predictive nanotoxicological assessment. *Curr. Drug Metab.* 16, 932–939. <https://doi.org/10.2174/1389200216666151015113720>.
- Tajes, M., Eraso-Pichot, A., Rubio-Moscardo, F., Guivernau, B., Bosch-Morato, M., Valls-Comamala, V., Muñoz, F.J., 2014. Methylglyoxal reduces mitochondrial potential and activates Bax and caspase-3 in neurons: implications for Alzheimer's disease. *Neurosci. Lett.* 580, 78–82. <https://doi.org/10.1016/j.neulet.2014.07.047>.
- Ulusoy, M., Lavrentieva, A., Walter, J.G., Sambale, F., Green, M., Stahl, F., Scheper, T., 2016. Evaluation of CdTe/CdS/ZnS core/shell quantum dot toxicity on three-dimensional spheroid cultures. *Toxicol. Res.* 5 (1), 126–135. <https://doi.org/10.1039/c5tx00236b>.
- Vicente Miranda, H., Szego, É.M., Oliveira, L.M.A., Breda, C., Darendeligiolu, E., de Oliveira, R.M., Ferreira, D.G., Gomes, M.A., Rott, R., Oliveira, M., Munari, F., Enguita, F.J., Simões, T., Rodrigues, E.F., Heinrich, M., Martins, I.C., Zamolo, I., Riess, O., Cordeiro, C., Ponces-Freire, A., Lashuel, H.A., Santos, N.C., Lopes, L.V., Xiang, W., Jovin, T.M., Penque, D., Engelender, S., Zweckstetter, M., Klucken, J., Giorgini, F., Quintas, A., Outeiro, T.F., 2017. Glycation potentiates alpha-synuclein-associated neurodegeneration in synucleinopathies. *Brain* 140 (5), 1399–1419. <https://doi.org/10.1093/brain/awx056>.
- Wang, Z., Wang, S.N., Xu, T.Y., Miao, Z.W., Su, D.F., Miao, C.Y., 2017. Organoid technology for brain and therapeutics research. *CNS Neurosci. Ther.* 23 (10), 771–778. <https://doi.org/10.1111/cns.12754>.
- Wang, Y.H., Yu, H.T., Pu, X.P., Du, G.H., 2014. Myricitrin alleviates methylglyoxal-induced mitochondrial dysfunction and AGEs/RAGE/NF- κ B pathway activation in SH-SY5Y cells. *J. Mol. Neurosci.* 53 (4), 562–570. <https://doi.org/10.1007/s12031-013-0222-2>.
- Wilson III, D.M., Cookson, M.R., Van Den Bosch, L., Zetterberg, H., Holtzman, D.M., Dewachter, I., 2023. Hallmarks of neurodegenerative diseases. *Cell* 186 (4), 693–714. <https://doi.org/10.1016/j.cell.2022.12.032>.
- Woodbury, D., Reynolds, K., Black, I.B., 2002. Adult bone marrow stromal stem cells express germline, ectodermal, endodermal, and mesodermal genes prior to neurogenesis. *J. Neurosci. Res.* 69 (6), 908–917. <https://doi.org/10.1002/jnr.10365>.
- Xu, J., Chen, L.J., Yu, J., Wang, H.J., Zhang, F., Liu, Q., Wu, J., 2018. Involvement of advanced glycation end products in the pathogenesis of diabetic retinopathy. *Cell Physiol. Biochem.* 48 (2), 705–717. <https://doi.org/10.1159/000491897>.
- Xu, K., Zhang, L., Yu, N., Ren, Z., Wang, T., Zhang, Y., Zhao, X., Yu, T., 2023. Effects of advanced glycation end products (AGEs) on the differentiation potential of primary stem cells: a systematic review. *Stem Cell Res. & Ther.* 14 (1), 74. <https://doi.org/10.1186/s13287-023-03324-5>.
- Xue, M., Rabbani, N., Thornalley, P.J., 2011. Glyoxalase in ageing. *Semin. Cell. Dev. Biol.* 22 (3), 293–301. <https://doi.org/10.1016/j.semcdb.2011.02.013>.
- Xue, M., Momiji, H., Rabbani, N., Barker, G., Bretschneider, T., Shmygol, A., Rand, D.A., Thornalley, P.J., 2015. Frequency modulated translocational oscillations of Nrf2

- mediate the antioxidant response element cytoprotective transcriptional response. *Antioxid. Redox Signal.* 23, 613–629. <https://doi.org/10.1089/ars.2014.5962>.
- Yang, Z., Zhang, W., Lu, H., Cai, S., 2022. Methylglyoxal in the brain: from glycolytic metabolite to signalling molecule. *Molecules* 27 (22), 7905. <https://doi.org/10.3390/molecules27227905>.
- Zakrzewski, W., Dobrzyński, M., Szymonowicz, M., Rybak, Z., 2019. Stem cells: Past, present, and future. *Stem Cell Res. Therap.* 10 (1), 68. <https://doi.org/10.1186/s13287-019-1165-5>.
- Zhang, H., Li, H., Xi, H.S., Li, S., 2012. HIF1alpha is required for survival maintenance of chronic myeloid leukemia stem cells. *Blood* 11, 2595–2607. <https://doi.org/10.1182/blood-2011-10-387381>.
- Zhao, M., Lewis Wang, F.S., Hu, X., Chen, F., Chan, H.M., 2017. Acrylamide induced neurotoxicity in primary astrocytes and microglia: roles of the Nrf2-ARE and NF-Kb pathways. *Food Chem. Toxicol.* 106 (Pt A), 25–35. <https://doi.org/10.1016/j.fct.2017.05.007>.